Magnet System Considerations for a Compact Compression Boosted Ignition Test Reactor

H. Becker, E. Bobrov, L. Bromberg, D.R. Cohn,
D. Hay, F. Malik, D.B. Montgomery
M. Olmstead, J. Schultz, M. Sniderman,
C. Weggel and J.E.C. Williams

September 1978
Plasma Fusion Center Report # RR-78-10

Magnet System Considerations for a Compact Compression Boosted Ignition Test Reactor[†]

H. Becker, E. Bobrov, L. Bromberg, D. R. Cohn,
D. Hay, F. Malik[*], D. B. Montgomery,
M. Olmstead, J. Schultz[*], M. Sniderman[*],
C. Weggel and J. E. C. Williams

M.I.T. Plasma Fusion Center[††]
and
Francis Bitter National Magnet Laboratory[‡]

Plasma Fusion Center Report RR-78-10

† Work supported by U.S. D.O.E. Contract ET-78-S-02-4646

* Westinghouse Fusion Power Systems Department

†† Supported by U.S. D.O.E

‡ Supported by N.S.F.

Table of Contents

1.0 Introduction and Summary

Objectives and Motivations

The purpose of a copper magnet ignition test reactor is:

to demonstrate ignition

to study alpha particle physics in a regime where alpha particle heating dominates over all other heating

to study the control of an ignited plasma over an extended period of time (10-20 sec).

A compact copper magnet ignition test reactor is attractive because it affords the possibility of meeting these goals in the mid 1980s at moderate cost. The development of a compact device is facilitated by a Bitter plate magnet design which allows for high stress and a choice of insulation such that shielding is not required for the *TF* coils. The use of compression to reduce neutral beam requirements for penetration allows the use of state of the art 120 kev D^0 beams. The confidence level for heating to ignition is thus very significantly enhanced over reliance on rf heating or yet to be developed negative ion neutral beams.

A concept for a compression boosted high field ignition test reactor was discussed in MIT Plasma Fusion Center Research Report RR-78-4.[1] In the present report further parametric studies of this concept are described and magnet engineering design considerations are discussed. The work described here should be directly relevant to the compression boosted copper magnet ignition test reactor design under consideraton by the Garching and Frascati groups.[2]

Parametric Studies

The additional parametric studies described in this report indicate that optimal designs for a compression boosted copper ignition test reactor may be characterized by lower toroidal fields at the ignited plasma. A point design for a device with a field of 10 T at the ignited plasma (in contrast

to 12.5 T in MIT Plasma Fusion Center Research Report RR-78-4) has been developed. The parameters of this point design are given in Table 1.1. The major radius of the ignited plasma (R = 1.27 m) and the physical size of the Bitter magnet are essentially unchanged. However, the reduction to 10 T of the magnetic field at the ignited plasma does result in a decrease of ~30% in the stored energy of the toroidal field magnet.

The parametric studies were carried out for fixed maximum vertical stress and bending stress in the Bitter magnet. The values of these stresses were held constant at 2.9 10^8 P (40 kpsi). The ratio of copper to stainless steel in the throat of the magnet is assumed to be 2:1. The stress in the copper is 2.1 10^8 P (30 kpsi). In general, the present parametric studies show that, for fixed stress levels of 2.9 10^8 P (40 kpsi), there is a region of rather flat dependence upon magnetic field at the major axis of the ignited plasma of the magnet stored energy, neutral beam power, equilibrium field power requirements and the physical dimensions of the magnet. This flat dependence between 8 and 10 T results from an increase in plasma size and a decrease in aspect ratio (leading to higher values of toroidal beta) with decreasing magnetic field.

The flat top period of the *TF* coil is calculated by assuming that the limiting effect is the temperature rise of the *TF* coil. The maximum allowable temperature before shut-off is 400°K. Flat top periods generally exceed 20 seconds for 2.9 10^8 P (40 kpsi) stress levels.

The margin of ignition parametric studies indicate a strong sensitivity of crucial magnet parameters to the distance between the inner edge of the toroidal field coil and the edge of the plasma. A distance of 10 cm has been chosen for the point design presented in this report. This distance is consistent with the preliminary vacuum chamber design concept which has been developed.

Compression Requirements

Estimates have been made of the distortion of the vertical field by eddy currents produced in the copper Bitter plates. It is found that if a 2 cm (3/4") thick copper plate is used the maximum deviaton in the vertical field is ~4% . The maximum deviaton occurs approximately 20 ms after the

initiation of the compression stroke.

The effect of the vertical field index n upon the energy swing requirements for the vertical field system has been determined. For an index of 0.4, the required energy swing for the design in Table 1.1 is 70 MJ. For n = 1.0 the energy swing requirement is reduced to 50 MJ. The peak power requirement is approximately 800 MW. The 1/e time for the compression is 50 ms.

A design has been developed for an inductive energy storage system for a 100 MJ, 50 ms equilibrium field energy swing. This system involves cryogenically cooled copper Bitter coils with separate leads. The coils are charged in series and discharged in parallel through a resistor and the load coil. The capital cost of the inductive storage and energy transfer systems is estimated to be 10.5 M.

Toroidal Field Coil Design

The toroidal field coil construction consists of liquid nitrogen cooled Bitter plates with ports formed by perturbation of the plates. The Bitter plate design uses steel reinforced copper. Cryogenic grade oxygen free electronic (*OFE*) copper is utilized. *OFE* copper has excellent electrical conductivity and is available in plates as wide as 3.5 m. A comparison of the strength and electrical conductivity characteristics of stainless steel reinforced copper relative to various copper alloys has been made. Stainless steel reinforced copper still appears to be the best choice. However, a materials evaluation program is highly desireable in order to gain further information about the possible use of copper alloys.

A study has been made of the possible types of insulation which could be utilized. Candidate materials are either completely inorganic or partly organic. Inorganic materials offer high resistance to neutron damage but have poor cyclic mechanical properties. Partly organic materials have good mechanical properties but are more susceptible to radiation damage. The best choice appears to be mica which should be useable for 10^{11} rad (~50,000 burn seconds). The mica would probably have to be enclosed in protective aluminum or steel sheets because of its poor mechanical properties.

The present point design could be operated for as long as a 22 s flat top pulse. In this case the toroidal field coil would receive approximately 4. 10^9 J of heat from ohmic heating and neutron bombardment. Approximately 26,000 liters of LN_2 would be needed to recool to 77°K. For a 10 second flat top the amount of heat could be reduced to 1.5 10^9 J and only 10,000 liters of nitrogen would be needed for cooling.

The Bitter plate magnet would require a series current of 250 kA and a peak voltage of 600 volts. This magnet is matched to the peak power but not to the impedance of the transformer/rectifier at the Max Planck Institute for Plasma Physics at Garching.

Toroidal Field Magnet Fabrication

The toroidal field magnet would consist of 256 turns each consisting of a single piece copper plate and a steel reinforcing plate made up of four subsized pieces. The steel and the copper would be keyed to produce equal strain in the copper and the steel. Insulator plates would be made from mica bonded between protective aluminum or steel sheets.

There would be eight 45 cm square horizontal injecton ports. More modest vertical access for diagnostics would be incorporated into eight split flanges. The port design would consist of 3 turns bent away to provide an opening. Higher current density turns adjacent to the ports help to compensate the magnetic field ripple produced by the opening. This design approach was employed in the neutral beam heated *ALCATOR* upgrade (*HFBT*) design where the toroidal ripple was kept at sufficiently low values.

The overall magnet assembly is patterned after *ALCATOR C* in order that practical experience obtained in the construction of that device can be carried over into the constructon of the copper ignition reactor.

The Bitter plate toroid would be made up of eight loosely stacked modules of Bitter plates. Each module of plates along with a 45° section of vacuum vessel is held together by its own assembly until fiberglass bands and clamps pull them together into a solid structure.

Maintenance of the copper ignition test reactor would involve replacement of a complete octant module.

Vacuum Chamber

Preliminary consideration has been given to the use of a thin walled vacuum chamber with bellows, which obviates the need for a ceramic break. The bellows both increases the electrical resistance and provides for distribution of the heat generated by the alpha particles. The bellows would be about 2 mm thick and 5 cm deep. Cooling of the bellows could be provided by a surrounding stagnant water jacket. For the plasma parameters in the present design the heat flux into the water jacket would be on the order of 20 Watts/cm^2. This value is sufficiently low to insure good heat transfer. A 10 s burn would involve a rise in water temperature on the order of 20^o C. The water jacket would provide an additonal means of tritium containment.

An alternative to the water jacket is an internally shielded vacuum vessel in which the shield resembles one extended limiter around the plasma and acts as an inertial thermal sink, also protecting the vacuum wall against plasma disruptions.

References

1 L. Bromberg, D. R. Cohn and J. E. C. Williams, MIT Plasma Fusion Center Research Report 78-4 (April 1978)

2 Compact Ingnition Experiment Internal Status Report, prepared by Max Plank Institut fur Plasmaphysik, Garching and the Divisone Fusione of CNEN, Frascati (1978)

TABLE 1.1

Design Parameters

Mag. field at final plasma B_t	10 T
Major radius of final plasma R	1.27 m
Minor radius of final plasma a	0.43 m
Central plasma temperature T(o)	15 keV
Central plasma density n(o)	8×10^{14} cm^3
Average (β_t)	3.8%
Current of final plasma I	3 MA
Compression ratio	2
Neutral beam energy	120 keV D^o
Neutral Beam Power	13 MW
Inductive Energy of TF mag	1.2×10^9 joules
TF coil flat top	22 sec
Peak power of TF magnet	150 MW
$\frac{n\tau_E}{(n\tau_E)_{ign}}$ at $\beta_T \approx 3.8\%$	1
$\left(\frac{n\tau_E}{n\tau_E}\right)_{ign}$ at $\beta = \beta_{critical} = 5.4\%$	2

2. Parametric Study

In this section we perform a parametric study in order to investigate the TF coil.

The plasma performance of an ignition experiment is best described by using two margins of safety: the margin of safety of ignition for beams and the margin of ignition for beta. The margin of safety of beams MI_{beams} is determined by the beam penetration. The maximum value of $n_o\, a$, where n_o is the plasma density on axis and a is the plasma minor radius at which a peaked beam deposition profile can be obtained is given by[1]

$$n_o\, a \approx 1.1\ 10^{14}\, W_b\, C^{3/2}\, cm^{-2} \tag{2.1.1}$$

where W_b is in keV and C is the compression ratio. The margin of safety of ignition for beams is defined by

$$MI_{beams} = \frac{(n_o\tau_e)_{emp,\,beam}}{(n_o\tau_e)_{ign}} = \frac{4.6\ 10^9\, W_b^2\ C^3}{(n_o\tau_e)_{ign}} \tag{2.1.2}$$

where τ_e is the energy confinement time and $(\, n_o\tau_e\,)_{ign}$ is the value of $n_o\tau_e$ at ignition. The global energy confinement time has been assumed to be the empirical confinement time, $\tau_e = \tau_{e,\,emp}$ [2]. It has been determined that for most of the range of parameters described here, $\tau_{i,\,nc} > \tau_{e,\,emp}$, where $\tau_{i,\,nc}$ is the neoclassical energy confinement time for the ions [3].

Similarly, the margin of safety for beta is determined by the maximum value of β_T allowed by the plasma stability. It has been assumed that the maximum value of β_T is given by [4]

$$\beta_{T,crit} = \frac{1}{A\ q_a^2} \tag{2.1.3}$$

where A is the plasma aspect ratio and q_a is the safety factor at the limiter. The margin of safety due to beta is then

$$MI_{beta} = \frac{(n_o\,\tau_e)_{max\ beta}}{(n_o\,\tau_e)_{ign}} \sim \beta_{crit}^2\ B_T^4\ a^2 \sim \frac{B_T^4\ a^2}{A^2} \sim \frac{(I_p\, A)^4}{R_f^2} \tag{2.1.4}$$

where B_T is the magnetic field on axis and R_f is the plasma major radius. It will be shown that because of the high power of $I_p A$ in the equation for MI_{beta}, the parameter $I_p A$ is determined more by the desired value of MI_{beta} than by the alpha containment requirement, which also depends on $I_p A$. [5] In order to allow for some temperature excursion of the ignited plasma or to allow for a decreased value of $\beta_{T,crit}$, $MI_{beta} \approx 2$.

The profile of the plasma density has been assumed parabollic. The temperature profile is somewhat flater, based on recent *ALCATOR* results at $q \sim 2.5$. The plasma temperature has been assumed to be 15 keV on axis. Decreasing the plasma temperature to 13 keV increases MI_{beta} by ~ 5% at the cost of reducing MI_{beams} by ~ 20 %. It has been assumed that the percentage of the alpha particles contained in the system is determined by an uniform current profile in the plasma. As more realistic peaked profiles produce better alpha containment properties, this is a conservative assumption. (As the effect of toroidal ripple on the alpha particles is not well understood, this provides for some safety). As stated above, the desired MI_{beta} determines the value of $I_p A$.

With these simplifications, the plasma properties can be describes by the two parameters MI_{beta} and MI_{beams}. Another important parameter is the required neutral beam power, P_{beams} not only because the beams represent a significant fraction of the total cost, but because the beam power determines the necessary access. In Bitter type magnets this should be reduced to a minimum. The beam power is calculated assuming that the compression is truly adiabatic. In the next section this assumption will be relaxed to find a tradeoff between peak compression power and neutral beam power.

The main stresses in the TF coil are the tensile stresses in the throat of the TF coil σ_{TF}, and the bending stresses in the horizontal section of the coil, σ_{bend}.

Assuming that the tensile stresses in the throat of the TF magnet are uniform (this is approximately true for the *ALCATOR C* tokamak[6]) the tensile stresses in this region are given by

$$\sigma_{TF} = \frac{\frac{3}{2\pi} M_T - \frac{R_o^3 - R_b^3}{\pi (R_o^2 - R_b^2)} F_T}{R_a^3 - R_1^3 - \frac{R_o^3 - R_b^3}{R_o^2 - R_b^2} (R_a^2 - R_1^2)} \qquad (2.1.5)$$

where F_T and M_T are respectively the total upward force and the moment due to the magnetic field and are given by

$$F_T = \frac{\pi B_f^2 R_f^2}{\mu_o} \left(ln(\frac{R_b}{R_a}) + \frac{1}{4}(1 - \frac{R_1}{R_a})^2 + (1 - \frac{R_1}{R_a}) \frac{R_1}{3 R_a} \right) \qquad (2.1.6)$$

and

$$M_T = \frac{\pi B_f^2 R_f^2}{\mu_o} \left(R_b - R_a + (R_a - R_1) \left[\frac{1}{5}(1 - \frac{R_1}{R_a})^2 + \frac{R_1}{2 R_a}(1 - \frac{R_1}{R_a}) + \frac{1}{3}(\frac{R_1}{R_a})^2 \right] \right) \qquad (2.1.7)$$

We have assumed that the magnetic field increases linearly in the throat of the magnet and that the forces generated in the outer throat of the magnet are small (the results change by ~ 1% when included). R_a and R_b are given by

$$R_a = R_f - a_f - \delta_f,$$

$$R_b = R_i + a_i + \delta_i,$$

where R_i and R_f are the initial and final major radii of the plasma, a_i and a_f are their corresponding minor radii, and δ_i and δ_f are the distances between the plasma edge and the TF coil of the precompressed plasma and of the compressed plasma. R_o and R_1 are the maximum and minimum radii of the TF coil, respectively (see Fig. 2.1.1).

The maximum bending stresses are determined by calculating the bending moments in the horizontal legs of the magnet and then calculating the corresponding bending stress using elementary theory of beams. It is found that the bending stresses are relatively flat in this region for $R_f < R < R_i$. The height of the magnet that results in a maximum bending stress of 2.9 10^8 P (40 10^3 psi) is then determined.

The stored magnetic energy is calculated in two parts: the energy inside the TF bore and the energy in the TF conductor. The energy in the TF bore can be calculated analytically. The energy in the TF conductor is calculated numerically. This energy contribution depends on the current distribution in the TF coil, but changes by only 5% as the current distribution goes from uniform everywhere to $\sim r^{-1}$ at the throat and uniform elsewhere. In typical Bitter type magnets, the energy stored in the conductor region of the TF magnet is ~ 60-70% of the energy in the bore.

The pulse length is calculated assuming that the limiting effect is the temperature rise of the TF coil. The largest temperature rise occurs in the throat of the magnet. Assuming that the maximum allowable temperature before shut-off is 400 K then the allowed pulse length is [6]

$$\tau_{flat} = \frac{\langle J^2 \tau \rangle}{J_{TF}^2} F_{Cu} - \frac{1}{3} \tau_{rise} = \frac{8.\ 10^8\ (A\ cm^{-2})^2\ s}{J_{TF}^2} F_{Cu} - \frac{1}{3} \tau_{rise} \qquad (2.1.8)$$

where J_{TF} is the current density in the copper and F_{Cu} is the percentage of the volume that is occupied by copper. τ_{rise} is the time neccesary for the TF current to reach the flat top value. This is valid if the resistive power during the current rise time is small compared with the inductive power. When the plasma achieves ignited operation, the neutrons contribute to heating of the TF coil. It has been estimated that this effect will reduce the flat top of the pulse by ~ 25% (see section 4.3) . The percentage of copper in the inboard of the TF coil, F_{Cu} is partially determined by the stresses in this region, and has been assumed to be 66%.

The resistive power in the TF coil, P_{tf} , is also calculated. This is only an approximate result, and assumes that the TF coil is at 77 K . More precise calculations are shown in section 4.3.

Finally, the volume V_{ol} of the conductor and structural material in the TF coil is calculated. This is indicative of the cost of the magnet.

In Table 2.1.1 the results of a parametric study are shown for I_pA = 8.7 10^6A . In the Table, BF is B_f in Tesla, R_f and a are in cm, height is the height of the TF coil in cm, I_p is the plasma current of the compressed plasma, W_{me} is the stored energy in the TF coil in J, P_{tf} and

P_{beams} are in W and V_{ol} is in cm^3. τ_{flat} is in s, W_b is in keV. Stf and Sbend are σ_{TF} and σ_{bend} and are given in psi. Finally, df is δ_f. The stresses in the TF magnet in Table 2.1.1 are σ_{TF} = σ_{bend} = 2.9 10^8 P (40 kpsi) . The percentage of copper in the throat of the magnet is 66%. This number determines both the maximum stresses in the throat of the magnet and the pulse length. The inner radius of the TF coil, R_1, is set to 0.25 m. Also, δ_f = 0.10 m and δ_i = 0.15 m (see Figure 2.1.1). The numbers in Table 2.1.1 are obtained by varying the minor radius of the plasma in the compressed state, and then finding the value of the toroidal field on axis of the compressed plasma from

$$B_f = \frac{2\pi}{\mu_o} \frac{q\, I_p\, A}{a} \qquad (2.1.9)$$

The major radius that results in σ_{TF}= 2.9 10^8 P (40 kpsi) is found. The height of the magnet is determined by the constraint σ_{bend} = 2.9 10^8 P (40 kpsi) . From Table 2.1.1, the minimum size magnet that ignites with $MI_{beta} \approx 2$ and MI_{beams} = 1 is $R_o \approx$ 3.4 m. As the magnetic field on axis decreases, the stored magnetic field in the TF coil decreases rapidly for B_f > 11 T and slower for lower fields. MI_{beta} peaks at $B_f \approx$ 9.5 T. As B_f decreases, the weight of the TF coil decreases (the volume of the TF conductor and structural material, V_{ol}, decreases). The plasma current I_p, on the other hand, increases due to a decrease in aspect ratio. The resistive power in the TF coil, P_{tf}, also decreases as B_f is lowered. For B_f < 10.0T, however, W_{me}, V_{ol}, P_{tf} vary slowly as the field is decreased further. Actually, R_o could be somewhat smaller and still satisfy MI_{beams} = 1. Not indicated in Table 2.1.1 are $\tau_{e,\,emp}$ and $\tau_{i,\,nc}$. For B_f < 11 T and R_o = 3.48 m, $\tau_{e,\,emp}$ > $\tau_{i,\,nc}$. As the magnetic field is reduced further, the current of the compressed plasma increases and, as $\tau_{i,\,nc} \sim I_p^2$, the ratio $\tau_{i,\,nc}/\tau_{e,\,emp}$ increases.

As R_o increases keeping $MI_{beams} \approx$ constant, MI_{beta} decreases somewhat. For $MI_{beams} \approx$ constant, the stored magnetic energy W_{me} and the resistive power P_{tf} also decrease. The volume of the TF coil conductor and structure V_{ol} does not change significantly, despite of the fact that the major radius of the coil, R_o , is increasing.

Tables 2.1.2 and 2.1.3 show similar results as Table I for I_pA = 9.5 10^6 A and I_pA =

8. 10^6 A . As previously stated, Ml_{beta} depends strongly on $I_p A$. If $Ml_{beta} \approx 2$, then $I_p A \approx 8.7$ 10^7 A.

Table 2.1.4 shows the same results as Table 2.1.1, but for δ_f = 0.15 m. The machine size increases significantly, and, to keep Ml_{beat} = 2, $I_p A$ has also to increase (due to an increase in R_f; see equation 2.1.4) . Table 2.1.5 shows results of the parametric study for δ = 0.07 m . Comparing Tables 2.1.1, 2.1.4 and 2.1.5 it is concluded that δ_f is an important variable, and further work should try to find its minimum realistic value (see section 6) .

In Table 2.1.6 the strong dependence of the TF coil parameteres on δ_f is shown. The case of B_f = 10.0 T has been chosen because in Tables 2.1.1, 2.1.4 and 2.1.5 the TF coil parameters do not change drastically for B_f < 10.0 T for the minimum size coil that results in $Ml_{beams} \sim 1$. The parameter $I_p A$ is changed to satisfy $Ml_{beta} \approx 2$. Shown in Table 2.1.6 are W_{me}, P_{tf}, P_{beams}, τ_{flat} and V_{ol} .

Table 2.1.7 shows results of the parametric study for σ_{TF} = 2.5 10^8 P (35 kpsi) . The other parameters are the same as for Table 2.1.1 . Ml_{beta} is ~ 10% smaller than the results in Table 2.1.1 . R_o has increased somewhat in order to keep the compression ratio constant ($C \approx 2$). The importance of having high stresses in the throat of the magnet is made clear by comparing Table 2.1.7 and 2.1.1 .

The results of the parametric study reveal that there is a wide range of parameters of the TF coil and the plasma that result in an ignition machine. Furthermore, for B_f in the range 8 - 10 T, the TF coil parameters are only slowly varying.

References

1 D. R. Cohn, D. L. Jassby and K. Kreischer, Nucl Fusion 18 1255 (1978)

2 D. R. Cohn, R. R. Parker and D. L. Jassby, Nucl. Fusion 16 31 (1976); D. L. Jassby, D. R. Cohn and R. R. Parker, Nucl. Fusion 16 1045 (1976)

3 F. L. Hinton and R. D. Hazeltine, Rev. Mod. Phys. 48 239 (1976)

4 A. M. M. Todd *et. al*, Phys. Rev. Lett. 38 826 (1977)

5 P. G. McALees, Oak Ridge National Laboratory Report ORNL-TM-4661 (1974)

6 C. Weggel *et. al*, in *Proceedings of the 7th Symposium on Engineering Problems of Fusion Research*, Knoxville, Tn, October 1977

1 D. R. Cohn, D. L. Jassby and K. Kreischer, Princeton Plasma Physics Laboratory Report MATT-1418 (1978), to be published in Nucl. Fusion

2 D. R. Cohn, R. R. Parker and D. L. Jassby, Nucl. Fusion 16 31 (1976); D. L. Jassby, D. R. Cohn and R. R. Parker, Nucl. Fusion 16 1045 (1976)

3 F. L. Hinton and R. D. Hazeltine, Rev. Mod. Phys. 48 239 (1976)

4 A. M. M. Todd *et. al*, Phys. Rev. Lett. 38 826 (1977)

5 P. G. McALees, Oak Ridge National Laboratory Report ORNL-TM-4661 (1974)

6 C. Weggel *et. al*, in *Proceedings of the 7th Symposium on Engineering Problems of Fusion Research*, Knoxville, Tn, October 1977

TABLE 2.1.1

df = 10.
WB= 120.0
IA= 8700000.0
R1= 25.0
Stf= 40000.0
Sbend= 40000.0
Fcu 0.666
T = 15.0

MSbeta	MSbeams	BF	a	R	HEIGHT	Ip	Wme	Ptf	Pbeams	VOL	Tflat
RO = 348.											
1.678	0.897	14.5	30.0	141.4	248.0	1.84E6	1.9E9	68.9E6	14.3E6	66.1E6	48.9
1.895	0.995	12.6	34.44	133.0	245.0	2.25E6	1.56E9	53.7E6	13.4E6	60.9E6	41.1
2.028	1.021	11.1	38.88	128.6	243.0	2.62E6	1.34E9	44.8E6	12.9E6	56.8E6	35.0
2.092	0.996	10.0	43.33	126.6	243.0	2.97E6	1.19E9	39.2E6	12.7E6	53.6E6	30.2
2.105	0.939	9.1	47.77	126.2	243.0	3.29E6	1.08E9	35.5E6	12.7E6	50.9E6	26.3
2.082	0.865	8.3	52.22	126.9	245.0	3.57E6	1.0E9	33.0E6	12.9E6	48.8E6	24.1
2.034	0.786	7.6	56.66	128.4	247.0	3.83E6	0.94E9	31.1E6	13.1E6	47.0E6	22.1
RO = 360.											
1.63	0.974	14.5	30.0	143.4	253.0	1.81E6	2.0E9	69.4E6	14.5E6	72.0E6	52.0
1.85	1.09	12.6	34.44	134.6	249.0	2.22E6	1.64E9	53.8E6	13.5E6	66.1E6	41.1
1.988	1.128	11.1	38.88	129.9	247.0	2.6E6	1.4E9	44.8E6	12.9E6	61.5E6	36.8
2.058	1.106	10.0	43.33	127.7	246.0	2.95E6	1.24E9	39.2E6	12.7E6	57.8E6	31.6
2.075	1.048	9.1	47.77	127.1	247.0	3.26E6	1.12E9	35.4E6	12.7E6	54.8E6	28.8
2.056	0.969	8.3	52.22	127.7	248.0	3.55E6	1.04E9	32.8E6	12.9E6	52.4E6	25.1
2.011	0.883	7.6	56.66	129.1	250.0	3.81E6	0.97E9	30.9E6	13.1E6	50.3E6	23.1
RO = 380.											
1.555	1.108	14.5	30.0	146.8	260.0	1.77E6	2.17E9	70.4E6	14.7E6	82.7E6	55.4
1.781	1.259	12.6	34.44	137.2	255.0	2.18E6	1.77E9	54.1E6	13.6E6	75.5E6	46.0
1.926	1.318	11.1	38.88	132.0	253.0	2.56E6	1.5E9	44.8E6	13.0E6	69.9E6	38.9
2.003	1.305	10.0	43.33	129.4	252.0	2.91E6	1.32E9	39.0E6	12.7E6	65.4E6	33.3
2.028	1.245	9.1	47.77	128.6	252.0	3.23E6	1.2E9	35.2E6	12.7E6	61.8E6	30.2
2.015	1.158	8.3	52.22	129.0	253.0	3.52E6	1.1E9	32.6E6	12.8E6	58.7E6	27.5
1.976	1.06	7.6	56.66	130.3	254.0	3.78E6	1.03E9	30.7E6	13.1E6	56.2E6	25.1
1.92	0.96	7.1	61.11	132.2	257.0	4.02E6	0.98E9	29.3E6	13.3E6	54.3E6	23.1

TABLE 2.1.2

df= 10.
WB= 120.0
IA= 9500000.0
R1= 25.0
Stf= 40000.0
Sbend= 40000.0
Fcu 0.6666
T= 15.0

MSbeta	MSbeams	BF	a	R	Height	Ip	Wme	Ptf	Pbeams	Vol	Tflat
RO= 360.0											
2.059	0.809	15.8	30.0	156.2	263.0	1.82E6	2.51E9	89.0E6	15.9E6	77.8E6	59.2
2.378	0.93	13.7	34.44	145.3	259.0	2.25E6	2.06E9	67.4E6	14.7E6	71.9E6	48.9
2.6	0.988	12.2	38.88	139.0	257.0	2.65E6	1.75E9	54.9E6	14.0E6	67.1E6	41.1
2.731	0.991	10.9	43.33	135.6	257.0	3.03E6	1.54E9	47.1E6	13.7E6	63.2E6	36.9
2.789	0.956	9.9	47.77	134.2	257.0	3.38E6	1.39E9	42.0E6	13.5E6	60.1E6	33.3
2.793	0.899	9.0	52.22	134.1	258.0	3.69E6	1.28E9	38.4E6	13.6E6	57.5E6	30.2
RO = 380.											
1.954	0.912	15.8	30.0	160.3	272.0	1.77E6	2.74E9	98.7E6	16.3E6	89.7E6	63.4
2.278	1.066	13.7	34.44	148.5	267.0	2.2E6	2.23E9	68.1E6	14.9E6	82.4E6	55.4
2.508	1.146	12.2	38.88	141.5	264.0	2.6E6	1.89E9	55.1E6	14.1E6	76.5E6	46.1
2.649	1.162	10.9	43.33	137.7	263.0	2.98E6	1.65E9	47.1E6	13.7E6	71.8E6	41.1
2.717	1.131	9.9	47.77	135.9	263.0	3.33E6	1.49E9	41.8E6	13.6E6	67.9E6	35.0
2.73	1.07	9.0	52.22	135.6	263.0	3.65E6	1.36E9	38.2E6	13.6E6	64.7E6	31.7
2.702	0.992	8.3	56.66	136.3	265.0	3.94E6	1.27E9	35.6E6	13.7E6	62.1E6	30.2
2.647	0.909	7.7	61.11	137.7	266.0	4.21E6	1.2E9	33.7E6	14.0E6	59.8E6	27.5
RO = 400.											
2.423	1.318	12.2	38.88	144.0	271.0	2.56E6	2.02E9	55.3E6	14.2E6	86.8E6	48.9
2.573	1.348	10.9	43.33	139.7	269.0	2.94E6	1.77E9	47.1E6	13.8E6	81.0E6	43.5
2.65	1.322	9.9	47.77	137.7	268.0	3.29E6	1.58E9	41.7E6	13.6E6	76.3E6	38.9
2.671	1.259	9.0	52.22	137.1	269.0	3.61E6	1.45E9	38.0E6	13.6E6	72.5E6	35.0
2.65	1.174	8.3	56.66	137.6	270.0	3.9E6	1.35E9	35.3E6	13.7E6	69.3E6	31.7
2.602	1.08	7.7	61.11	138.9	271.0	4.17E6	1.27E9	33.4E6	13.9E6	66.5E6	28.8
2.534	0.984	7.2	65.55	140.8	274.0	4.42E6	1.21E9	32.0E6	14.2E6	64.4E6	27.5

TABLE 2.1.3

df= 10.
WB= 120.0
IA= 8000000.0
R1= 25.0
Stf= 40000.0
Sbend= 40000.0
Fcu= 0.6666
T= 15.0

MSbeta	MSbeams	BF	a	R	Height	Ip	Wme	Ptf	Pbeams	Vol	Tflat
RO = 335.											
1.361	0.951	13.3	30.0	129.0	233.0	1.85E6	1.44E9	54.8E6	13.0E6	55.5E6	38.9
1.5	1.014	11.6	34.44	122.9	231.0	2.24E6	1.2E9	43.9E6	12.3E6	51.1E6	31.7
1.573	1.009	10.2	38.88	120.0	230.0	2.59E6	1.03E9	37.5E6	12.0E6	47.8E6	27.5
1.596	0.958	9.2	43.33	119.2	230.0	2.9E6	0.92E9	33.4E6	12.0E6	45.1E6	24.1
1.584	0.884	8.3	47.77	119.6	231.0	3.19E6	0.84E9	30.7E6	12.1E6	43.0E6	22.2
RO = 350.											
1.316	1.065	13.3	30.0	131.2	239.0	1.82E6	1.54E9	55.1E6	13.1E6	62.0E6	41.1
1.46	1.15	11.6	34.44	124.6	235.0	2.21E6	1.27E9	43.9E6	12.4E6	56.8E6	35.0
1.538	1.153	10.2	38.88	121.4	234.0	2.56E6	1.09E9	37.4E6	12.0E6	52.8E6	30.2
1.566	1.103	9.2	43.33	120.3	234.0	2.88E6	0.97E9	33.3E6	12.0E6	49.7E6	26.3
1.558	1.023	8.3	47.77	120.6	235.0	3.16E6	0.89E9	30.5E6	12.1E6	47.2E6	23.1
1.527	0.93	7.6	52.22	121.9	236.0	3.42E6	0.82E9	28.6E6	12.3E6	45.1E6	21.3
RO = 370.											
1.41	1.344	11.6	34.44	126.8	241.0	2.17E6	1.36E9	44.0E6	12.4E6	64.8E6	36.9
1.495	1.363	10.2	38.88	123.1	240.0	2.52E6	1.17E9	37.3E6	12.0E6	60.0E6	31.7
1.529	1.315	9.2	43.33	121.8	239.0	2.84E6	1.04E9	33.1E6	11.9E6	56.2E6	27.5
1.526	1.228	8.3	47.77	121.9	240.0	3.13E6	0.94E9	30.3E6	12.0E6	53.0E6	25.2
1.499	1.123	7.6	52.22	123.0	241.0	3.39E6	0.88E9	28.4E6	12.2E6	50.5E6	23.1
1.456	1.013	7.0	56.66	124.8	243.0	3.63E6	0.82E9	27.0E6	12.5E6	48.5E6	21.3
1.404	0.906	6.5	61.11	127.1	247.0	3.84E6	0.78E9	26.1E6	12.9E6	47.7E6	19.7

TABLE 2.1.4

df= 15.
WB= 120.0
IA= 8900000.0
R1= 25.0
Stf= 40000.0
Sbend= 40000.0
Fcu= 0.6666
T= 15.0

MSbeta	MSbeams	BF	a	R	Height	Ip	Wme	Ptf	Pbeams	Vol	Tflat
RO = 370.0											
1.49	0.83	14.8	30.0	158.1	263.0	1.68E6	2.37E9	82.0E6	16.1E6	81.4E6	59.2
1.703	0.943	12.9	34.44	147.9	258.0	2.07E6	1.95E9	62.7E6	15.0E6	74.9E6	48.9
1.848	0.992	11.4	38.88	142.0	256.0	2.43E6	1.66E9	51.5E6	14.3E6	69.8E6	41.1
1.931	0.99	10.2	43.33	138.9	255.0	2.77E6	1.46E9	44.4E6	14.0E6	65.6E6	36.9
1.966	0.953	9.3	47.77	137.6	255.0	3.08E6	1.32E9	39.7E6	13.9E6	62.3E6	33.3
1.965	0.895	8.5	52.22	137.7	256.0	3.37E6	1.22E9	36.5E6	14.0E6	59.5E6	30.2
RO = 390.											
1.422	0.938	14.8	30.0	161.8	271.0	1.64E6	2.57E9	83.1E6	16.4E6	93.3E6	63.4
1.64	1.081	12.9	34.44	150.7	265.0	2.03E6	2.1E9	63.1E6	15.1E6	85.5E6	52.0
1.79	1.151	11.4	38.88	144.3	262.0	2.39E6	1.78E9	51.5E6	14.4E6	79.2E6	46.1
1.88	1.16	10.2	43.33	140.8	261.0	2.73E6	1.56E9	44.3E6	14.0E6	74.2E6	38.9
1.921	1.124	9.3	47.77	139.3	260.0	3.05E6	1.41E9	39.5E6	13.9E6	70.1E6	35.0
1.925	1.062	8.5	52.22	139.1	261.0	3.34E6	1.29E9	36.2E6	14.0E6	66.7E6	31.7
1.904	0.986	7.8	56.66	139.9	262.0	3.6E6	1.2E9	33.8E6	14.1E6	63.8E6	28.8
RO = 410.											
1.736	1.323	11.4	38.88	146.5	268.0	2.36E6	1.9E9	51.6E6	14.5E6	89.4E6	48.9
1.832	1.344	10.2	43.33	142.6	266.0	2.7E6	1.66E9	44.2E6	14.0E6	83.4E6	43.5
1.879	1.312	9.3	47.77	140.8	266.0	3.01E6	1.49E9	39.3E6	13.9E6	78.5E6	36.9
1.888	1.247	8.5	52.22	140.4	266.0	3.3E6	1.37E9	36.0E6	13.9E6	74.4E6	33.3
1.871	1.163	7.8	56.66	141.1	267.0	3.57E6	1.27E9	33.5E6	14.1E6	71.0E6	31.7
1.835	1.07	7.2	61.11	142.5	268.0	3.81E6	1.2E9	31.8E6	14.3E6	68.0E6	28.8
1.787	0.976	6.7	65.55	144.4	272.0	4.03E6	1.14E9	30.5E6	14.6E6	66.3E6	26.3

TABLE 2.1.5

df = 7.
WB= 120.0
IA= 8500000.0
Rl= 25.0
Stf= 40000.0
Sbend= 40000.0
Fcu= 0.6666
T= 15.0

MSbeta	MSbeams	BF	a	R	Height	Ip	Wme	Ptf	Pbeams	Vol	Tflat
RO = 335.											
1.77	0.962	14.1	30.0	130.4	238.0	1.95E6	1.61E9	60.2E6	13.2E6	57.4E6	41.1
1.975	1.045	12.3	34.44	123.5	236.0	2.37E6	1.33E9	47.6E6	12.4E6	52.9E6	35.0
2.091	1.052	10.9	38.88	120.0	235.0	2.75E6	1.14E9	40.3E6	12.0E6	49.4E6	30.2
2.135	1.008	9.8	43.33	118.7	235.0	3.1E6	1.02E9	35.7E6	11.9E6	46.7E6	26.3
2.129	0.936	8.8	47.77	118.9	236.0	3.41E6	0.93E9	32.6E6	12.0E6	44.5E6	23.1
2.088	0.85	8.1	52.22	120.1	237.0	3.69E6	0.86E9	30.5E6	12.2E6	42.7E6	21.3
RO = 350.											
1.917	1.18	12.3	34.44	125.3	241.0	2.33E6	1.41E9	47.8E6	12.4E6	58.9E6	36.9
2.04	1.199	10.9	38.88	121.5	239.0	2.72E6	1.21E9	40.3E6	12.0E6	54.8E6	31.7
2.091	1.158	9.8	43.33	120.0	239.0	3.06E6	1.07E9	35.6E6	11.9E6	51.5E6	27.5
2.091	1.081	8.8	47.77	120.0	240.0	3.38E6	0.98E9	32.5E6	12.0E6	48.9E6	25.2
2.056	0.987	8.1	52.22	121.0	241.0	3.66E6	0.91E9	30.3E6	12.2E6	46.8E6	22.2
1.998	0.889	7.5	56.66	122.8	243.0	3.92E6	0.85E9	28.8E6	12.4E6	45.0E6	20.5
RO = 370.											
1.846	1.372	12.3	34.44	127.7	247.0	2.29E6	1.52E9	48.0E6	12.5E6	67.3E6	41.1
1.977	1.412	10.9	38.88	123.4	245.0	2.67E6	1.3E9	40.2E6	12.0E6	62.3E6	35.0
2.037	1.376	9.8	43.33	121.6	244.0	3.02E6	1.15E9	35.4E6	11.9E6	58.4E6	30.2
2.044	1.294	8.8	47.77	121.4	245.0	3.34E6	1.04E9	32.3E6	11.9E6	55.1E6	26.3
2.015	1.189	8.1	52.22	122.2	246.0	3.63E6	0.96E9	30.1E6	12.1E6	52.5E6	24.1
1.963	1.076	7.5	56.66	123.8	248.0	3.88E6	0.91E9	28.5E6	12.4E6	50.4E6	22.2
1.896	0.964	6.9	61.11	126.0	251.0	4.12E6	0.86E9	27.4E6	12.7E6	48.8E6	20.5

Table 2.1.6

δ_f	W_{me}	P_{beams}	P_{TF}	Vol	T_{flat}
0.07	1.04	12.0	36	47	27
0.10	1.2	12.7	39	54	30
0.15	1.4	14	44	65	36

df= 10.
WB= 120.0
IA= 8900000.0
Rl= 25.0
Stf= 35000.0
Sbend= 40000.0
Fcu= 0.6666
T= 15.0

MSbeta	MSbeams	BF	a	R	Height	Ip	Wme	Ptf	Pbeams	Vol	Tflat
RO = 365.											
1.74	0.924	12.9	34.44	146.3	252.0	2.09E6	1.84E9	57.6E6	14.8E6	70.4E6	59.2
1.906	0.985	11.4	38.88	139.8	250.0	2.47E6	1.57E9	46.9E6	14.1E6	65.6E6	48.9
2.006	0.991	10.2	43.33	136.3	249.0	2.82E6	1.38E9	40.3E6	13.7E6	61.7E6	43.5
2.051	0.959	9.3	47.77	134.7	250.0	3.15E6	1.24E9	35.9E6	13.6E6	58.5E6	38.9
2.056	0.903	8.5	52.22	134.6	251.0	3.45E6	1.14E9	32.9E6	13.6E6	55.9E6	35.0
2.032	0.834	7.8	56.66	135.4	253.0	3.72E6	1.07E9	30.7E6	13.8E6	53.8E6	31.7
RO = 380.											
1.685	1.023	12.9	34.44	148.7	257.0	2.06E6	1.96E9	58.0E6	15.0E6	77.9E6	63.4
1.856	1.1	11.4	38.88	141.7	255.0	2.44E6	1.66E9	47.1E6	14.2E6	72.3E6	52.0
1.961	1.116	10.2	43.33	137.8	254.0	2.79E6	1.45E9	40.3E6	13.8E6	67.7E6	46.1
2.012	1.086	9.3	47.77	136.1	254.0	3.12E6	1.31E9	35.8E6	13.6E6	64.1E6	41.1
2.021	1.028	8.5	52.22	135.8	255.0	3.42E6	1.2E9	32.7E6	13.6E6	61.0E6	36.9
2.001	0.954	7.8	56.66	136.4	257.0	3.69E6	1.12E9	30.5E6	13.8E6	58.5E6	33.3
RO = 400.											
1.793	1.264	11.4	38.88	144.2	261.0	2.4E6	1.78E9	47.3E6	14.3E6	81.9E6	55.4
1.904	1.294	10.2	43.33	139.9	259.0	2.75E6	1.55E9	40.3E6	13.8E6	76.4E6	48.9
1.961	1.27	9.3	47.77	137.8	259.0	3.08E6	1.39E9	35.7E6	13.6E6	71.9E6	43.5
1.977	1.209	8.5	52.22	137.3	260.0	3.38E6	1.27E9	32.6E6	13.6E6	68.2E6	38.9
1.963	1.128	7.8	56.66	137.8	261.0	3.65E6	1.18E9	30.3E6	13.8E6	65.2E6	36.9
1.927	1.038	7.2	61.11	139.0	263.0	3.91E6	1.11E9	28.7E6	14.0E6	62.4E6	33.3
1.877	0.946	6.7	65.55	140.9	266.0	4.13E6	1.06E9	27.5E6	14.3E6	60.8E6	31.7

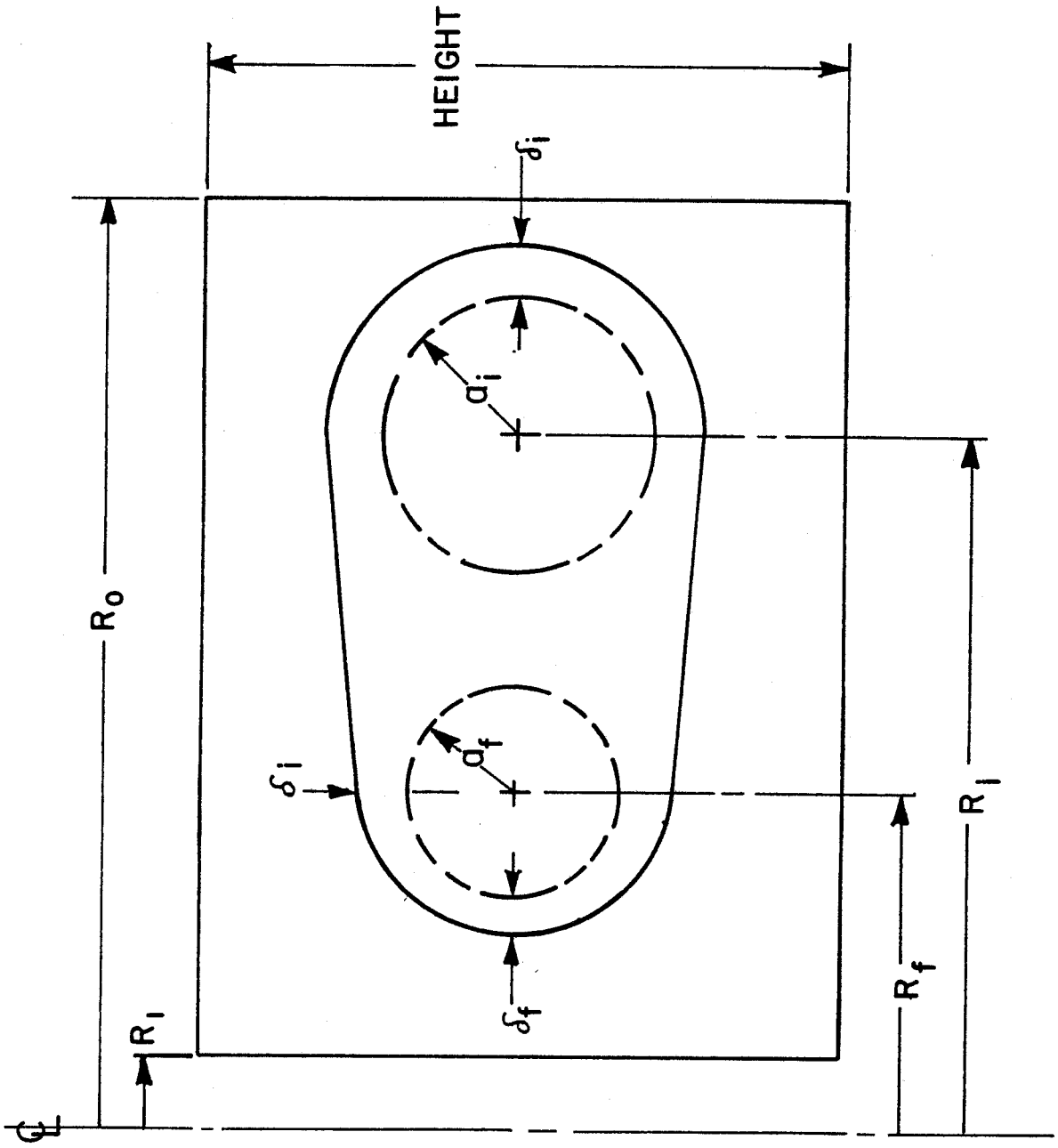

Figure 2.1.1 A schematic diagram of a Bitter Plate.

3. Vertical Field Considerations

3.1 Compression requirements

The compression of the plasma of the *HFITR* requires large transfers of energy in relatively short times. In this section we perform a parametric study to analyze the tradeoffs.

The calculations of beam power in the previous section have assumed infinitely fast compression times. By increasing the compression time, the peak power of the EF decreases, while the neutral beam power has to be increased because of plasma energy lost during compression. The beam power required prior to compression is shown in Figure 3.1.1 against the compression time. This Figure is drawn for R_f = 1.27, B_F = 10.0 T, a = 0.43 m, I_p = 3.1 10^6 A, T_f = 15 Kev, $C \sim$ 2.0. It is assumed that the plasma moves with a constant radial speed during compression. Although this is not the best compression scheme, the results do not depend strongly on it.

For compression times faster than 0.03 s, the compression is not collissional. The beam power required for $\tau_{comp} < 0.03$ s has not been calculated because of the large peak power required in the vertical system during compression.

On the other hand, the β-limit and the increase in neutral beam power impose the limit on how long the compression time can be. This is due to the higher initial temperatures necessary because of the slow compression to ignition. The ratio of β_t to β_{crit} is

$$\left(\frac{\beta_t}{\beta_{crit}} \right)_{initial} > \frac{1}{C^{5/6}} \left(\frac{\beta_t}{\beta_{crit}} \right)_{final} \qquad (2.1.1)$$

A compression time of ~75 ms requires a ~10% increase in beam power but allows for comfortable peak powers during compression (see below).

To calculate the energy required for compression, a computer program was developed that optimizes the current distribution in a system of coils (in terms of matching a given index of curvature on the midplane). The positions of the coils are varied until the stored energy is minimized while still matching (~10%) the specified index of curvature. It is concluded that there is

a relatively broad set of coil positions which results in comparable stored magnetic energy in the vertical field for a given index.

Three sets of coils are chosen for the parametric study. Although more coils would provide additional flexibility, the results described here are close to the optimum.

Figure 3.1.2 shows the increase in stored magnetic energy during compression against n, the index of curvature, defined by

$$n = -\frac{R}{B_z}\frac{dB_z}{dR} \qquad (2.1.2)$$

Figure 3.1.2 is calculated for R_F = 1.27, a = 0.43, B_T = 10.0 T, $I_p A$ = 8.7 10^6 A and C = 2. The energy in the EF system depends on the vertical distance of the outermost set of coils. In Figure 3.1.2, this distance is assumed to be 1.6 m.

It has been shown [1,2] that for radial and vertical stability, $0 < n < 1.5$ if the plasma is flux conserving, and $0 < n < 1$ if the plasma is not flux conserving. Therefore, although high n numbers result in a reduction of the change in stored energy in the vertical field, they may result in poor radial stability and decreased β_{crit}, as the plasma is elongated in the horizontal direction.[3] Furthermore, horizontal elongation decreases the allowable compression ratio for a fixed machine size. Although it results in ~40% larger energy swing (and, therefore ~40% larger peak power), n = 0.4 was chosen.

In order to include the vertical field properties in the parametric study of section 2.1, the change in the stored energy in the vertical field during compression has been calculated for different values of the magnetic field on axis. The TF coil and plasma parameters used are from Table 2.1.1 with R_o = 3.48 m. Figure 3.1.3 shows the change in stored magnetic energy in the vertical field against the toroidal field on axis. The two curves in Figure 3.1.3 are for two different values of the vertical distance between the outermost set of coils. The lower curve is for a distance of 1.4 m and the upper curve is for a distance of 1.6 m .

As the toroidal field on axis is lowered, the swing in the stored magnetic energy increases.

This is due to an increase in plasma current resulting from a decrease in the aspect ratio (for $I_p A \approx$ constant). The scattered points represent calculations for different coil positions, calculated in the way indicated above. The energy swing increases from ~53 MJ for B_f = 14.5 T to 80 MJ for B_f = 8.3 T. For comparison, the stored energy in the toroidal field decreases from 1.9 GJ at 14.5 T to 1.0 GJ at 8.3 T.

The peak power of the vertical field swing, however, does not relate directly to Figure 3.1.3 because the energy confinement time, τ_e, increases with decreasing toroidal field B_f. The peak power is shown in Figure 3.1.4 assuming that the compression time is 0.15 τ_e. It should be noted that the cost of the energy transfer system is determined more by the peak power than by the total energy swing (see section 3.3). The peak power is approximately constant as the toroidal field is lowered.

Table 3.1.1 shows the characteristics of the *OH* and the *EF* systems, calculated for the parameters of Figure 3.1.2. Figure 3.1.5 shows the structure of the vertical field for the case of Table 3.1.1.

A significant fraction of the precompression plasma inductive and resistive volt-s are provided by a leaky *OH* transformer that is not in the center of the *TF* coil. The initial current through the leaky *OH* is set so that the current in this system is zero prior to compression. Compression reduces the inductive V-s by about 1 V-s, allowing the charge-up of the central *OH* coil; this flux is used to drive the plasma in the ignited phase. About 0.8 V-s are required to drive the plasma during this phase.

3.2 Penetration of the Vertical Field

Proper calculation of the 3-dimensional eddy currents are complicated. However, an approximate analysis does provide significant insight.

We assume that the infinite parallel plane approximation is locally valid. A necessary condition for this approximation to be valid is that the spatial variations of the vertical field are small in a distance comparable with the plate thickness. Also, as the effect of the eddy currents should be small, the field in the copper conductor can be assumed to first order to be given by the vacuum field. The eddy currents can then be calculated and the perturbation (which sould be small) estimated. The process is repeated if the estimated perturbations are large.

The average field decrement inside the copper plate itself is

$$< B >_{Cu} = \frac{8}{\pi^2} (B_f - B_i) \sum_{n\ odd} \frac{1}{n^2} \frac{1}{1-n^2 \frac{\tau_r}{\tau_m}} (\exp(-t/\tau_r) - \exp(-n^2 t/\tau_m) \qquad (3.2.1)$$

where the applied vertical field is

$$B(r, t) = B_i(r) + (B_f(r) - B_i(r)) (1 - \exp(-t/\tau_r)) \qquad (3.2.2)$$

and

$$\tau_m = \frac{4 \mu_o a^2}{\pi^2 \rho_{Cu}} \qquad (3.2.3)$$

where a is the half thickness of the plate and ρ_{Cu} is the resistivity of copper at liquid nitrogen temperature. It has been calculated that the temperature of most of the magnet at the moment of compression is close to the initial temperature (see section 4.3).

The penetration time through the stainless steel structure is much faster than through the copper plates. Therefore, the penetration delay through the stainless steel has been neglected.

It has been assumed that none of the field excluded from the copper returns through the plasma. As this will probaly happen at the larger major radii, our calculations will overestimate the effect of the eddy currents in this region. Under these circumstances, the toroidal average of the

vertical field is just

$$\langle B \rangle = F_{Cu} \langle B \rangle_{Cu} \tag{3.2.4}$$

Figure 3.2.1 shows the average distortion of the vertical field against time for plates of different size. This distortion is calculated on the magnetic axis of the compressed plasma, which has the largest distortion (because the plate size is the thickest and the percentage of copper is the largest at this point). This figure has been drawn for an index of curvature of n = 0.4 and for R_f = 1.21 m, a_f = 0.433 m , R_1 = 0.25 m, and R_o = 3.48 m .

The index of curvature n changes because of the perturbation of the vertical field by the eddy currents. The change of n on axis is 15% for a = 0.01 m.

As the index n is increased, the maximum distortion for a fixed plate size decreases. This is shown in Figure 3.2.2, drawn for a plate half-thickness of a = 0.01 m . This occurs because as the index n increases, the magnetic field swing decreases.

The power lost due to eddy currents is calculated using the same approximation. For an infinite plate, the energy losses per unit area (integrated over the plate thickness) due to eddy currents are

$$W_{diss.eddy} = \rho_{Cu} \frac{4(B_f - B_i)^2}{\mu_o^2 a} \sum_{n\ odd}^{\infty} \frac{1}{(1-n^2\tau_r/\tau_m)^2} \left(\frac{\tau_r}{2} + \frac{\tau_m}{2n^2} - \frac{2}{\frac{1}{\tau_r} + \frac{1}{n^2\tau_m}} \right) \tag{3.2.5}$$

The energy lost for the case of n = 0.4 and the same parameteres as for Figure 3.2.1 is ~ 2.0 MJ.

The effect of the ripple of the vertical field in the regions close to the TF coil is unknown. However, the experience of *ALCATOR A* may be illustrative. This tokamak has thick copper shells with four toroidal cuts and two poloidal cuts. The shells are 0.01 m thick. The vertical field has significant toroidal perturbations which, as far as can be determined, do not produce deleterious effects on the plasma.

In conclusion, it seems that a plate half thickness of a = .01 m provides sufficiently fast field

penetration and produces negligible energy losses.

3.3 Inductive Energy Storage System for Compression

Compression of the plasma requires an increase in the stored energy of the *EF* system of about 70 MJ. This energy change must take place in a time of about 50 msec. To do this economically, an energy transfer system has been proposed which uses an auxiliary energy storage coil, along with a parallel switch and resistor, to transfer energy quickly to a load coil with no initial current (Figure 3.3.1). This characterization of the equilibrium field system is an oversimplification of the actual design problem, because of the interaction of the equilibrium field coils with each other, other coils, machine structures and the plasma. However, a design study which models the *EF* system as an inductor provides insight into the nature of the real design problem, prior to the final specifications of poloidal field system parameters.

Two basic methods of buffering the utility line from the Tokamak load during this sudden power demand surge have been investigated: inductive energy storage and mechanical energy storage. Conventional controlled rectifiers and homopolar generators have been examined as possible methods of charging inductive energy storage coils (Figures 3.3.2 and 3.3.3). Both controlled rectifiers and a.c. generators and a.c. generators with exciter control and diode rectifiers have been suggested as methods for transferring stored mechanical energy to the Tokamak load.

An energy storage inductor using a charging rectifier has been selected as the reference scheme.

3.3.1 Inductive Storage

The proposed energy transfer system is shown in Figure 3.3.2. The energy storage inductor, L_s, consists of a stack of copper, solenoidal Bitter coils with separate leads. The coils are charged in series through a rectifier and discharged in parallel through a resistor and the load coil. This arrangement matches the impedance of typical rectifier units with that of a preferred *EF* coil system.

The controlled rectifier charges L_s through the closed switches, S_i and S_s. When L_s is fully charged, the load interrupters S_c are closed. Simultaneously, the voltage on the controlled rectifier is reversed. This reduces the current through PS_c and S_i to zero so that S_i can be opened. The coil current now flows through S_c. (An alternative design is to use an uncontrolled diode rectifier for coil charging and to commutate current out of S_i with the counterpulsing circuit CC_2. This would probably require di/dt controlling inductors to prevent too much of the commutating current from passing through S_c and PS_c) When the current has been transferred to L_s and S_c, the series switches S_s are opened and the paralleling switches S_p are closed, placing all the coil submodules in parallel across the load coil. The interrupting switches S_c are then commutated by the counterpulsing circuits CC_1. The storage coil current is transferred to the resistors R_{sw} and then to the load. After a specified time, the desired amount of energy has been transferred to the load coil L_L. At that time, R_{sw} is shunted, either by S_s reclosing or by an auxiliary closing switch S_{ci}. An auxiliary closing switch would allow vacuum interrupters to operate close to their interruption rating or for thyristor switches to operate near their surge ratings. It would also allow S_p to be reopened and let the remaining energy in L_s be dumped in R_{sw} at room temperature. A high-current sustaining rectifier PS_{sust} will maintain load coil current during the burn period, for controllability of plasma position, and for allowing rapid shutdown at the end of burn. This high-current rectifier and its associated rectifier-transformer will be one of the most expensive components in the energy transfer system. (A more economical alternative might be separate sustaining windings in the EF coils driven by rectifier sets of higher impedance).

The reference system described above has the lowest projected costs of the four circuit alternatives considered. It does not involve any new or potentially unavailable technologies. Its principle disadvantage is that five times as many switches have to operate successfully on each shot as there are coil modules. This demands simple reliable switches. Key parameters of the reference energy transfer system are listed in Table 3.3.1. Projected switch ratings are shown in Table 3.3.2.

3.3.2 Homopolar Storage

The alternative inductive energy transfer system is shown in Figure 3.3.3. A homopolar generator is run up to speed between pulses. Modified circuit breakers, S_i, are closed and charge L_s in a relatively short time (<1 s). S_c is then opened and L_s discharges through R_{sw} and L_L. When L_L has the desired amount of energy, either S_c recloses or an auxiliary closing switch S_{ci} closes. Current in L_L is then maintained by a sustaining supply.

This system is somewhat simpler than the system with the charging rectifier. However, it requires an extra high-current switch S_i. The second system is simpler but homopolar generators of the required rating are not readily available today, (as evidenced by the recent failure of the Texas Tokamak project to procure a 200 MJ homopolar). Therefore, it is overly optimistic to assume their availability at this time. If the Canberra homopolar generator were available, an attractive first cost for a homopolar system might be possible.

A non-inductive energy transfer system is shown in Figure 3.3.4. Either a motor or a rectifier-inverter may be used for motoring the generator-flywheel up to speed between shots. Probably this system should share mechanical inertia with the line buffer which will be used with the TF coil charging circuit. The cost of the controlled rectifier alone is estimated to be over $20 M.

3.3.3 Trade Study

A trade study was conducted with different energy storage coil designs and different scenarios for the two inductive energy transfer systems discussed above. The parameters varied included the current density in the coils, the ratio of the $L/2R$ decay time to the energy transfer time, the allowable temperature rise in the cryoresistive coils and the choice of purchasing liquid nitrogen off-site or generating it on-site. The conclusions of the study are:

1. A reference design was selected with a predicted capital cost of $10.5 M and a life

time cost of $14.7 M (see Table 3.3.3).

2. The ratio of t/τ = 1.5 is predicted to be less expensive than t/τ = 3, because the larger storage coil is more than compensated by lower switch, bus and sustaining supply costs.

3. Higher current-density coils appear to lead to the lowest system costs up to the highest achievable coil stresses.

4. On-site liquid nitrogen refrigeration should be provided for the entire tokamak reactor system, including the energy storage coil.

5. Further cost optimization points towards a smaller temperature rise than 100 K and the use of cryoresistive aluminum in steel slots as the storage coil. However, with the present cost model, it does not appear that the cost can be reduced by more than a couple of million dollars from the reference cost. A more useful study would be one that modeled the entire poloidal field system.

6. The switches S_c will be either vacuum breakers or air blast breaker. Experience with and development of vacuum breakers has indicated that they would be acceptable. However, air blast breakers have some advantages: higher interruption capacity, resistance to arc damage, ability to commutate with high arc voltage (in the event of counterpulse failure).

7. If S_c does not reclose, solid-state interrupters are an attractive alternative. A budgetary estimate has been made by Westinghouse that a solid-state switching system could be provided for $3.3 M.

References

1 V. D. Shafranov and E. Yurchenko, Nucl. Fusion 8 329 (1968)

2 S. Yoshikawa, Phys. Fluids 7 278 (1964)

3 A. M. M. Todd *et. al*, Princeton University Plasma Physics Laboratory report MATT-1470 (1978)

TABLE 3.1.1

Coil Major Radii		
R_1 (m)		1.2
R_2 (m)		2.7
R_3 (m)		3.8
Coil Current	Initial	Final
I_1 (MA)	0.52	1.6
I_2 (MA)	0.22	0.66
I_3 (MA)	0.51	1.52
$n = -\frac{R}{B_v}\frac{dB_v}{dR}$		0.4
Initial energy (MJ)		9.3
Final energy (MJ)		83.
Increase in energy during compression (MJ)		74.
τ_{comp} (s)		$\lesssim$ 0.1
Peak Power (MW)		$\lesssim$ 800
Power Supply		Inductive Storage
EF contribution to V-s		
Initial		5.5 V-s
Final		5.3 V-s

TABLE 3.3.1

KEY PARAMETERS OF REFERENCE ENERGY TRANSFER SYSTEM

ENERGY IN STORAGE COIL, (MJ)	625.0
WEIGHT OF COPPER IN STORAGE COIL, (Mg)	53.1
PEAK TEMPERATURE RISE IN COIL, (°K)	100.0
CURRENT IN STORAGE COIL, (MA)	0.938
CURRENT IN 1 INTERRUPTER, (kA)	49.4
COIL CHARGING POWER, (MW)	98.6
CURRENT IN COIL AND SUSTAINING RECTIFIER, (MA)	0.375

TABLE 3.3.2

PROJECTED SWITCH RATINGS FOR HFITR
INDUCTIVE ENERGY TRANSFER SYSTEM

Switch	Switches/ System	Peak Current	Peak Voltage	Current-Carrying Time	Current Interrupted
S_I	1	$I_s(0)/N$	V_{max}	20-100 s	0
S_c	N	$I_s(0)/N$	V_{max}	~10 ms	$I_s(0)/N$
S_s	N	$I_s(0)/N$	V_{max}	20-100 s	0
S_p	2N	$I_s(0)/N$	$V_{charging}$	~50 ms	~0
S_{ci}	1	$I_L(t)$	V_{max}	1-10 s	0

TABLE 3.3.3

COST OF REFERENCE ENERGY TRANSFER SYSTEM

SUBSYSTEM	COST
CHARGING RECTIFIER	$ 0.90 M
ENERGY STORAGE COIL	$ 1.17 M
COUNTERPULSING CIRCUITS	$1.19 M
CRYOGENIC REFRIGERATORS	$ 1.57 M
SUSTAINING RECTIFIERS	$ 2.62 M
RECTIFIER-TRANSFORMERS	$ 0.75 M
BUSWORK	$ 2.25 M
SUBTOTAL, CAPITAL COSTS	$10.5 M
RENTAL, AIR-BLAST BREAKERS	$ 1.19 M
CRYOGENIC REFRIGERATION	$ 3.04 M
SUBTOTAL, OPERATING COSTS (30,000 SHOTS)	$ 4.2 M
TOTAL LIFETIME COST	$14.7 M

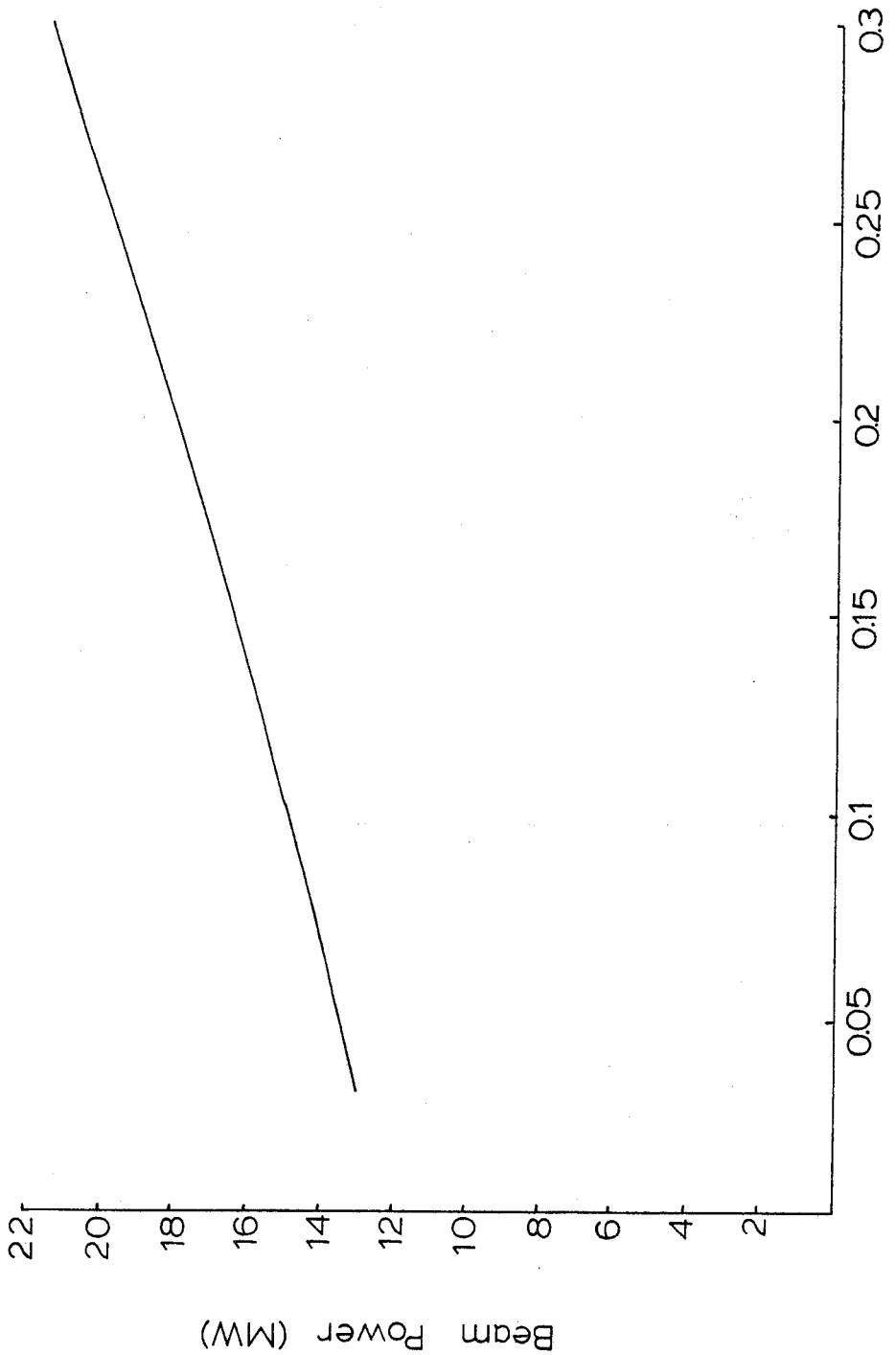

Figure 3.1.1 Neutral beam power against compression time.
B_T = 10.0 T

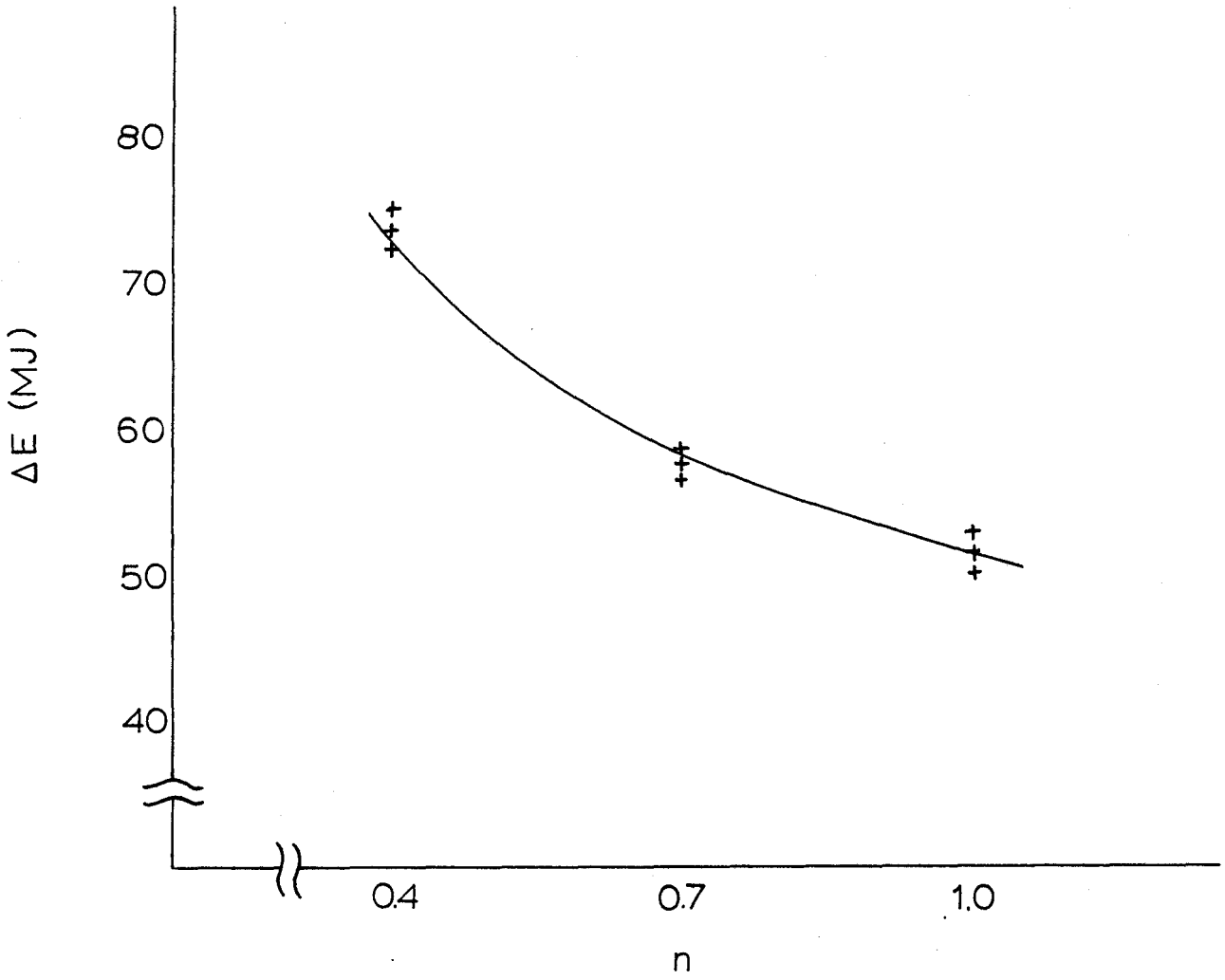

Figure 3.1.2 Change in stored energy in vertical system against index of curvature. B_T = 10.0 T

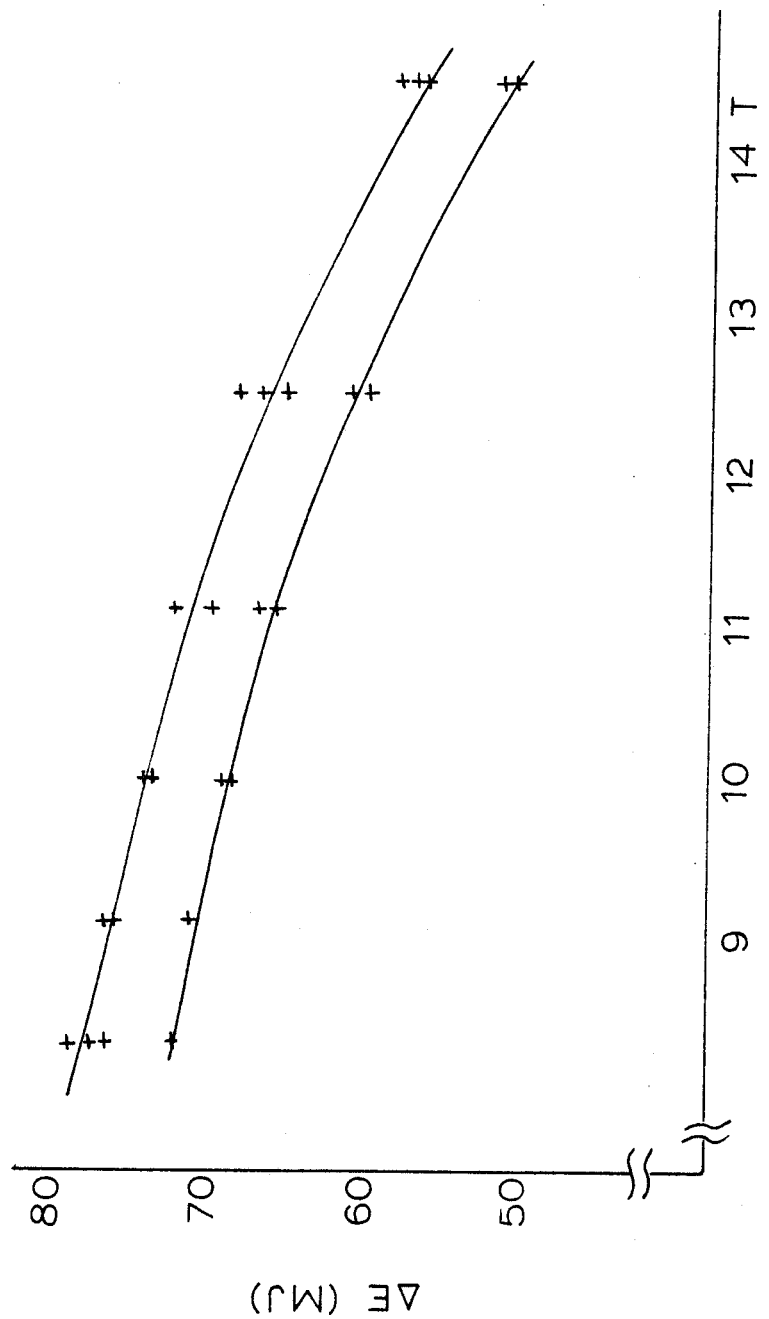

Figure 3.1.3 Change in stored energy in vertical field vs toroidal field on axis. R_o = 3.48 m.

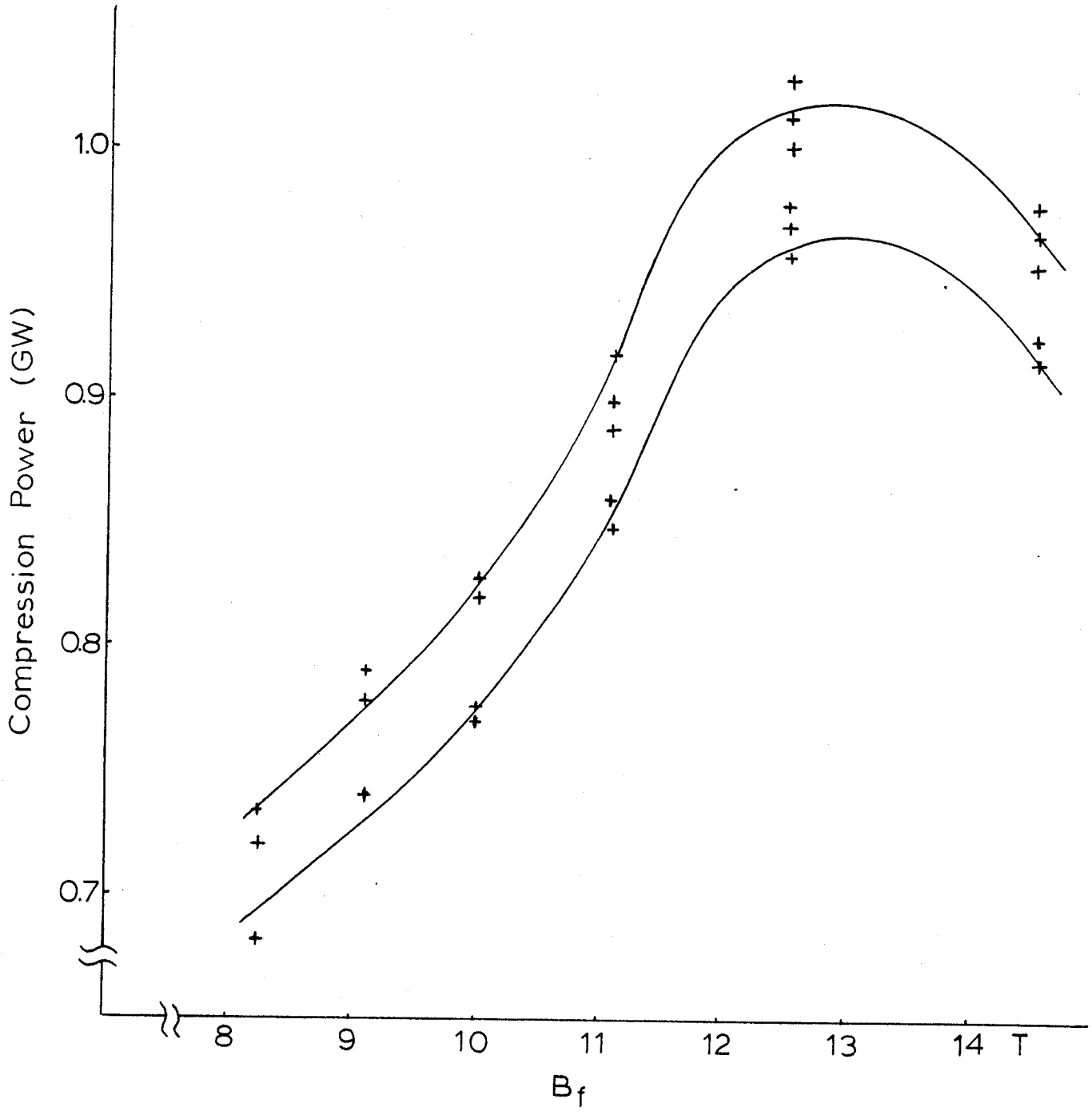

Figure 3.1.4 Compression Power vs toroidal field on axis. R_o = 3.48 m.

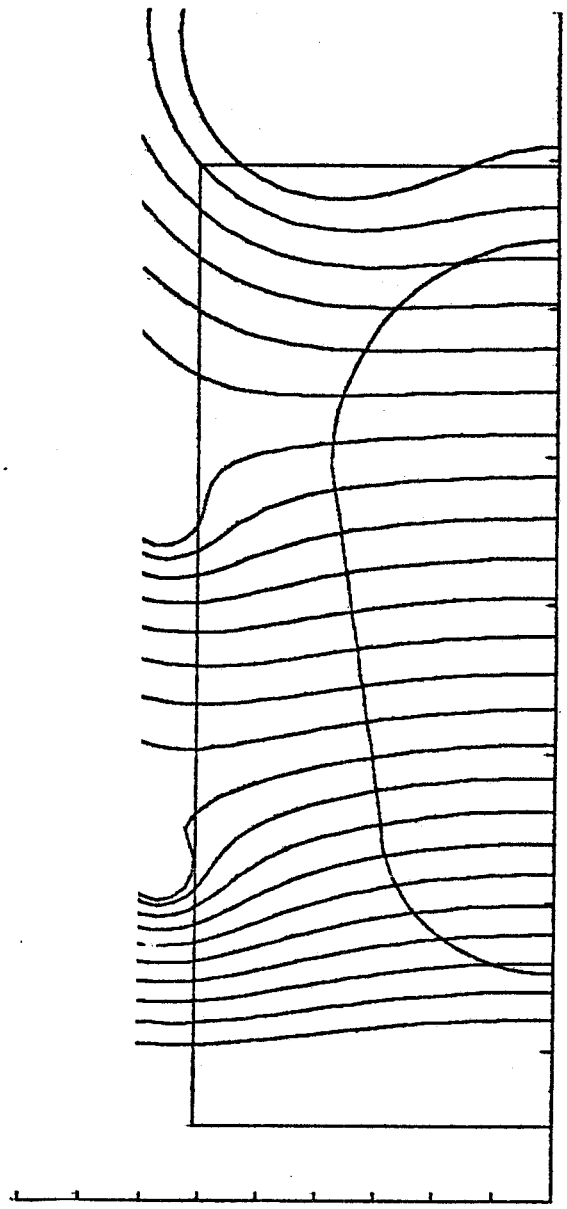

Figure 3.1.5 Structure of the vertical field.

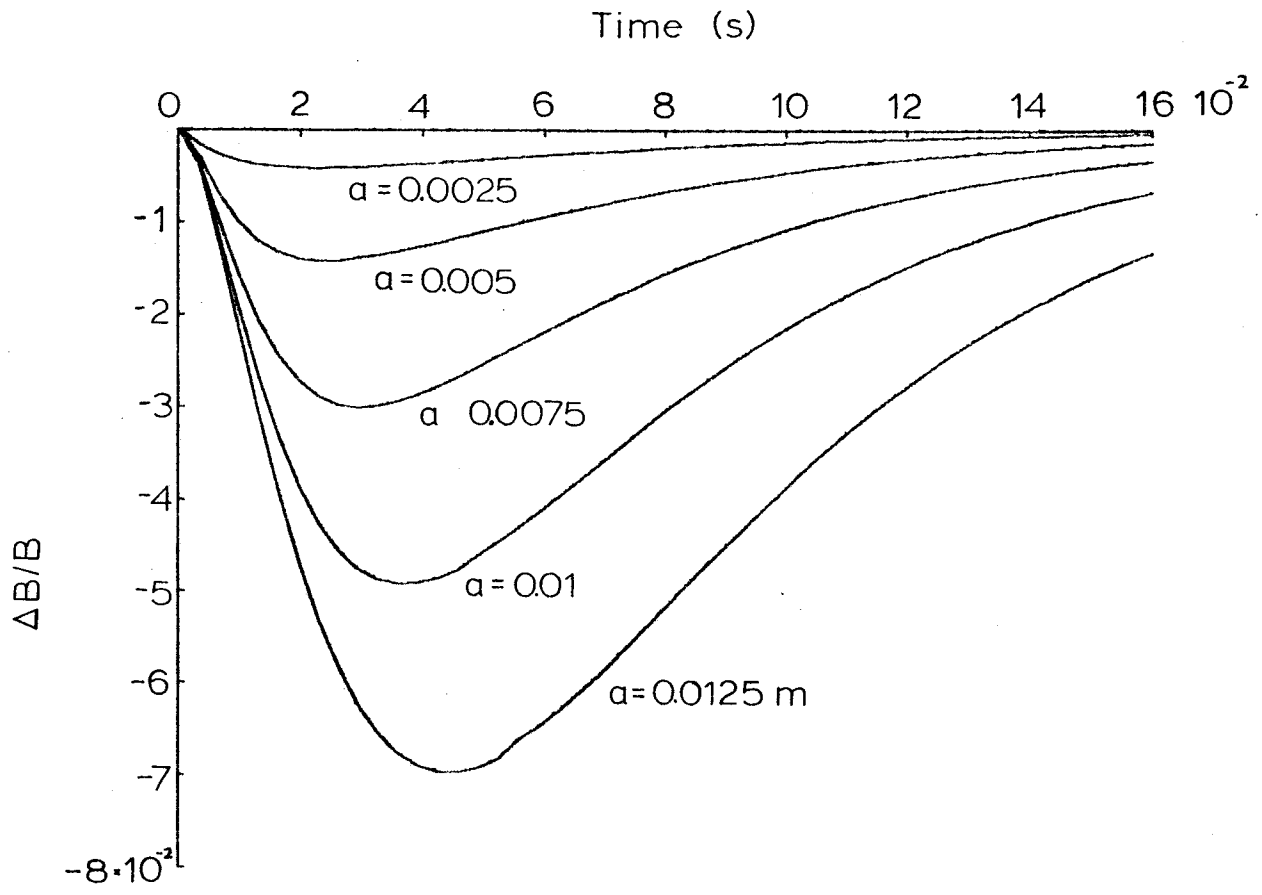

Figure 3.2.1 Perturbation of vertical field at R = 1.3 m; a is half-thickness of plate at $R \geq R_f$. B_T = 10. T

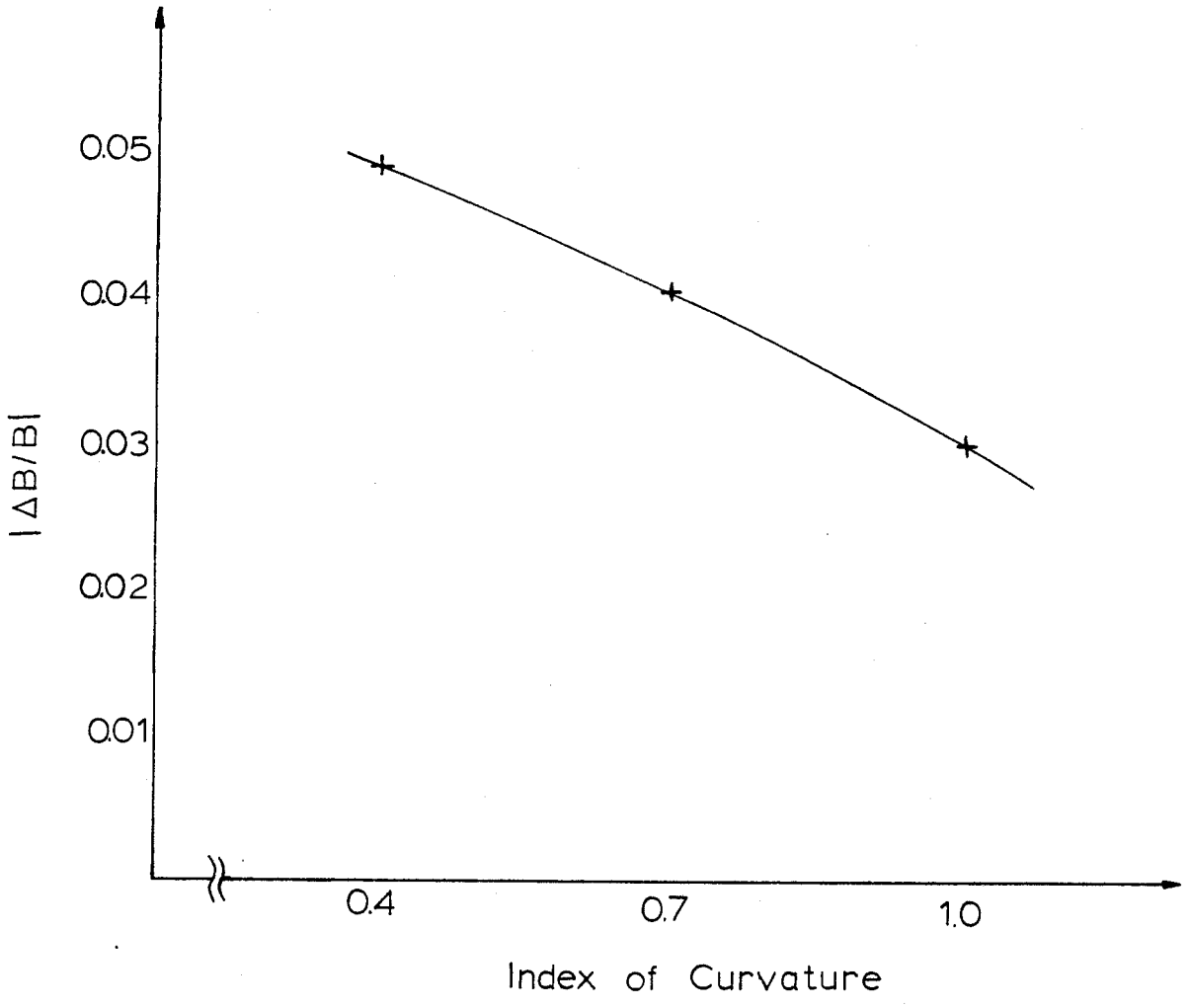

Figure 3.2.2 Perturbation of vertical field at R = 1.3 m. B_T = 10.0 T

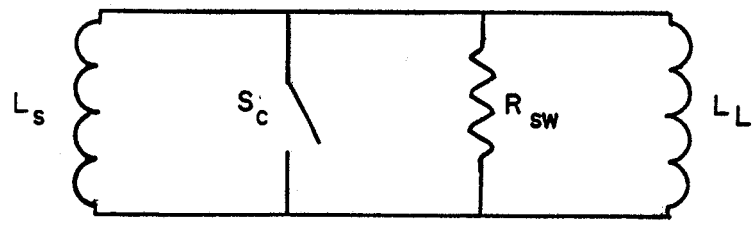

FIGURE 3.3.1 BASIC INDUCTIVE ENERGY TRANSFER SYSTEM

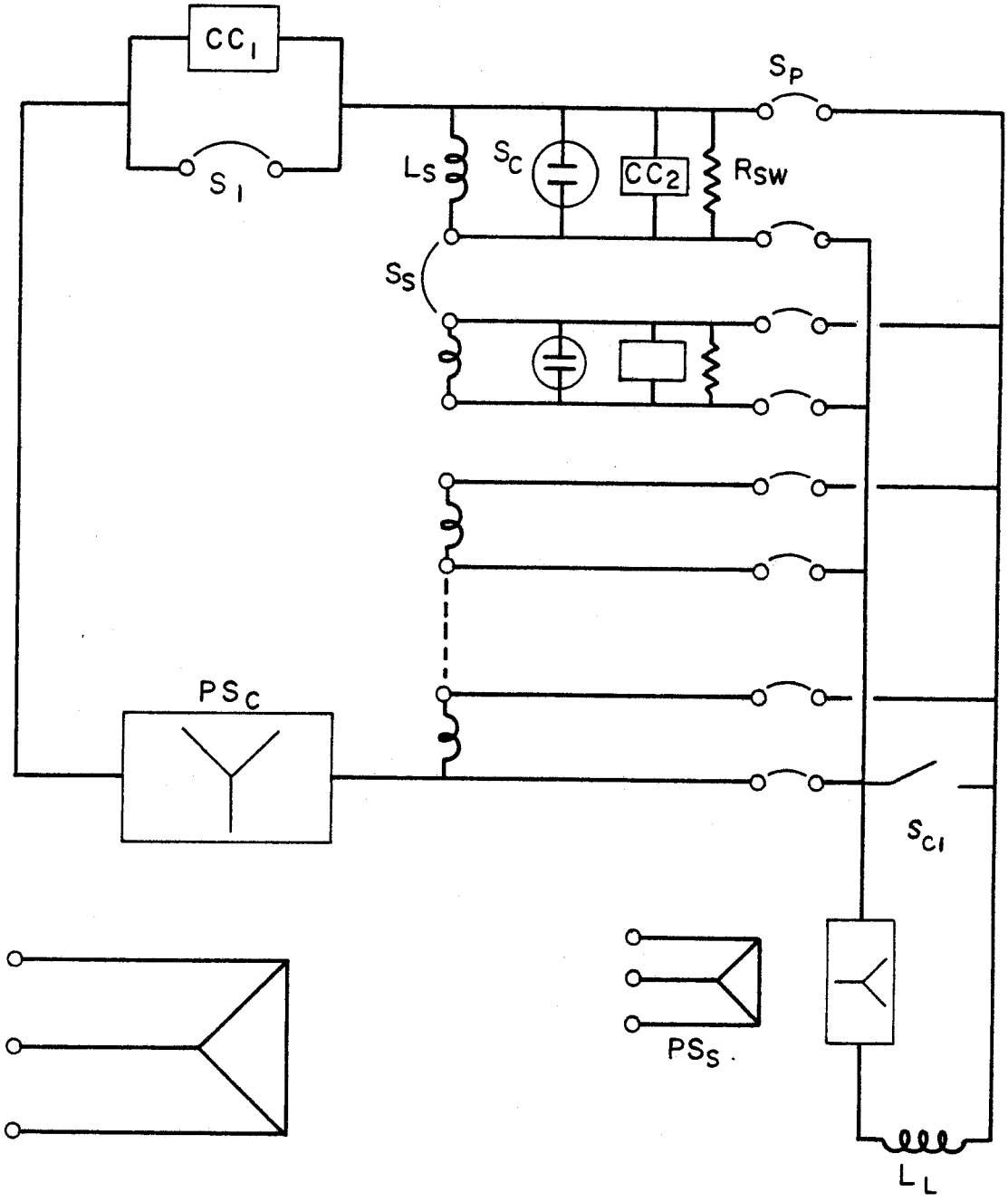

FIG. 3.3.2 PULSED POWER SUPPLY FOR COMPRESSION

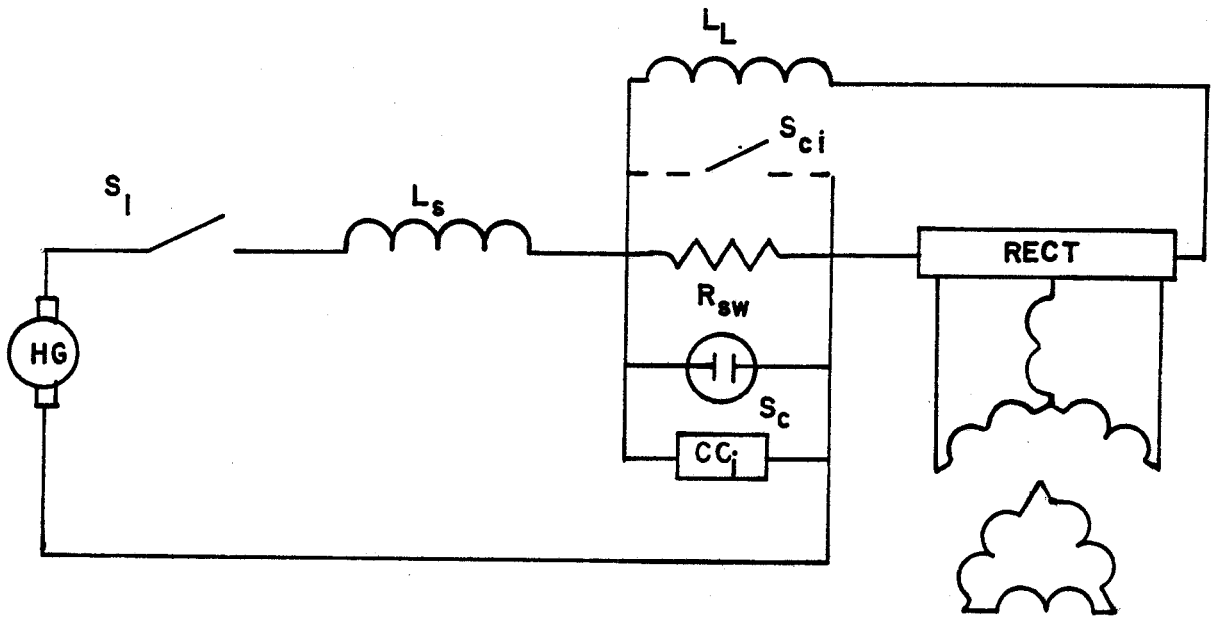

FIGURE 3.3.3 ALTERNATIVE INDUCTIVE ENERGY TRANSFER SYSTEM

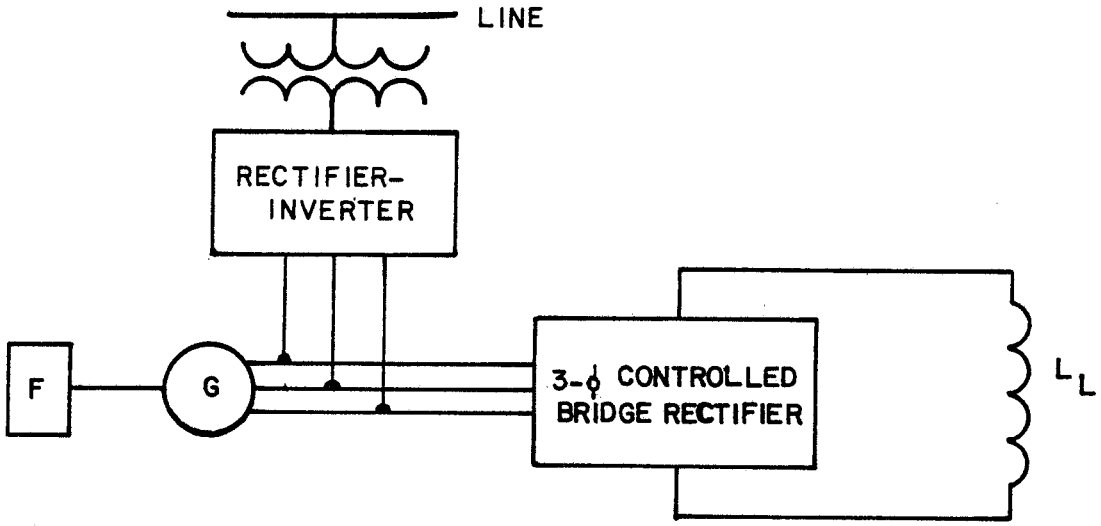

FIGURE 3.3.4 CONTROLLED-RECTIFIER WITH FLYWHEEL-GENERATOR LINE BUFFER

4.0 Toroidal Field Coil Design

4.1 Design Concept

The compression boosted high field approach to achieving ingition requires a magnetic field structure which uses LN_2 cooles Bitter magnets. The Bitter magnet concept appears to offer the most efficient structural approach, largely because the plates are monolithic in the direction of principle stresses. LN_2 cooling is used to permit high current density operation which facilitates the construction of a compact magnet.

We are proposing that the Bitter plates be reinforced with interleaved steel sheets and that the structure be pre-clamped by means of external tension bands as on the *ALCATOR C* machine.

We propose that the magnet be constructed in eight major sections with the turns distributed uniformly. The access ports would be formed by local perturbation of the plates rather than by gathering plates into subcoils as in more conventional approaches. A remote handling concept has been proposed in which any one-eighth sector could be removed for major repairs and replaced with a standby section.

4.2 Materials Selection

The critical area for any tokamak is in the inner leg where compromises must be made between conductivity and strength and between space devoted to the *TF* coil and space devoted to the plasma scrapeoff region and vacuum chamber. It has been our experience that steel-reinforced copper always has a better strength-conductivity performance than any alloy we have examined to date. During the past number of years, we have considered a number of promising high-strength, high-conductivity copper alloys which appeared to offer useful combinations of tensile strength and electrical conductivity. Table 4.2.1 presents our attempt at an exhaustive compilation of all potentially superior alloys. Unfortunately, relatively little data exists on the cryogenic properties of any of these alloys. What cryogenic data does exist, however, suggests that none of these alloys can surpass or even equal the combination of electrical conductivity and mechanical strength attainable with pure copper reinforced with ultra-high-strength stainless steel at 77°K. Nonetheless, before the final selection is made, a thorough materials-evaluation program should be undertaken.

4.2.1 The Electrical Conductor

Heavily cold-worked Cryogenic-Grade Oxygen-Free Electronic (*OFE*) Copper has been tentatively selected as the electrical conductor for all coil systems of the *ITR*. Its advantages include:

1. Excellent electrical conductivity, the best of any commercially available material. At room temperature, the electrical conductivity of *OFE* Copper is about 1% better than that of ordinary *ETP* Copper, and at liquid-nitrogen temperature, the improvement increases to approximately 8%
2. Satisfactory tensile and fatigue strength, when heavily cold-rolled to spring temper.
3. Superb ductility and toughness, even in this remarkably strong temper. As shown in table 4.2.2, its elongation-to-fracture is approximately 25%, far superior to that of ordinary *ETP* Copper of equal tensile strength.
4. Ready availability in large size plates. Plates as wide as 3.5 m are reported to be available

from at least 5 manufacturers.

5. It costs only $.15 per kg more than standard *ETP* Copper, all of whose properties it surpasses.
6. Excellent machinability and grindability.

The only two domestic suppliers of this material (whose official designation is Cryogenic Grade *CDA* 101) are Phelps-Dodge (Cryogenic- Grade *PDOF* Copper) and *AMAX* (Cryogenic Grade *OFHC* Copper).

4.2.2 The Mechanical Reinforcement

Wherever the strength of the copper is insufficient to withstand the local forces, it will be reinforced with steel. In the critical inner leg region reinforcement will be of heavily cold worked sheets of ultra-high-strength stainless steel. Carpenter Technology 18-18 Plus Stainless Steel (Aerospace Quality Electro-Slag-Remelted) has been tentatively selected for this purpose. An evaluation program for this material is already underway to confirm this choice. In addition to standard tensile tests, this program will include a variety of mechanical tests such as those of ductility, fatigue strength, impact toughness, and notch toughness.

As shown in Table 4.2.3, the initial results are encouraging. The advantages of this material include:

1. It is 100% austenitic at all temperatures, even when cold worked to very high levels of tensile strength.
2. As shown in Table 4.2.3, it is adequately strong, particularly at cryogenic temperatures
3. Despite its tensile strength, it appears to have adequate toughness and ductility, although the elongation-to-fracture data to substantiate this is inconclusive.
4. Being completely austenitic, it is nonmagnetic.
5. The alloy contains absolutely no nickel -- an element which is highly undesirable since under neutron bombardment nickel becomes activated, producing a radioactive isotope (Ni^{63}) with

a half-life of 85 years.

6. It is inexpensive; cheaper, in fact, than some conventional nickel-containing stainless steels.

A potential competitor is a stainless steel just now being developed by Foote Mineral Company. This is a stainless steel which contains neither nickel nor chromium. Its mechanical properties are presently being evaluated.

4.2.3 Electrical Insulation

The combination of high compressive pressure, large temperature excursions and intense nuclear radiation impose severe and unprecedented requirements on the electrical insulation between the Bitter plates of the *TF* coil. Table 4.2.4 lists the required design specifications.

In the *ITR* the loading will be cyclic so that extrusion, or cold flow, is unlikely to occur but fatigue characteristics of the insulator become critically important.

The insulation will also be subjected to linear stretching from the tensile strain in the adjacent plates. The resulting stress will be dependent on the elastic modulus of the insulation. No difficulty is expected from composite materials which generally have a low modulus, but oxide ceramics which are candidate insulating materials have a high modulus and are brittle as well. This suggests a different approach to the insulator configuration required according to the kind of material selected. A factor which must be considered is the circumferential compressive modulus and absolute reduction in thickness. This will affect the dynamic behaviour of the complete toroidal magnet assembly, particularly if it is large compared to the copper and stainless steel plates.

The primary neutron flux at the insulator is approximately 1.8 10^{15} n cm^{-2} sec^{-1} for a neutron power level of 63 MW. The source spectrum has a ~10% component at 14 MEV, but the bulk of the flux is substantially softened by the stainless steel and copper adjacent to the insulation. A mean energy of 0.1 MEV is assumed to be characteristic of the radiation reaching the insulation.

The maximum fluence of 50000 burn seconds (10^{20} n cm^{-2}) may be unnecessarily severe, but it represents 5000 cycles at 10 sec -- or 10000 cycles at 5 sec. The final decision on maximum

radiation limit is also affected by the fatigue properties of the insulation as well as its radiation resistance. The design limit of 5000 cycles does not include consideration for non-ignited operation (little or no radiation) or effects related to radiation damage enhancement under stress with a large temperature excursion. The fatigue limit of 20000 cycles was based on these characteristics.

4.2.3.1 Material Selection

Candidate materials are basically either completely inorganic or partly organic. The former offers high resistance to neutron damage but with poor cyclic mechanical properties. The latter have good mechanical properties which degrade under neutron bombardment at rates dependent on the fraction of organic polymer.

One of the more resistant organic materials, polymide, loses 50% of its tensile strength by 10^{10} rads of intermediate energy (0.1 MEV) neutron irradiation. In the range 1-5 10^{10} rad ceramics show a decrease in density due to swelling which is less than 1 volume % for the assumed design dose. The swelling leads to increased water absorbtivity, tensile strength, flectural strength and electrical conductivity. Permanent decreases of 1 to 2 orders of magnitude have been observed in the volume and surface resistivities of ceramic insulators, (Moisture absorption/content is significant but this is unlikely to be of major importance).

No significant effects except color darkening have been observed in most forms of mica irradiated to 10^{10} rad. However, some rigid inorganic bonded amber mica showed a 30% decrease in flexure at that dose, and the tensile strength of glass bonded mica decreased by 50% whereas the compressive strength remained unchanged. The electrical resistivity remained unchanged, though the dielectric constant increased by 20%.

Beyond 10^{10} rad there is a gradual decrease in thermal conductivity and density.

There is a significant difference between micas. Muskovite is less radiation resistant than phlogopite (amber) mica. Mica is readily available in large sizes with a completely inorganic binder. In manufacture these mica splittings are laminated with a silica compound and subsequently cured at

high pressure and temperature. The product is stiff (rigid), can be ground accurately to thickness, has excellent mechanical compressive load capacity (50000 psi) and excellent electrical properties. It resists extrusion under high compression. It has one characteristic typical of all mica materials which is a tendency to flake or crumble at the edges under abrasion or bending. This could be much reduced by bonding the mica to a stainless steel backing sheet or sandwiched between two sheets. Eiberglass reinforcing can also be incorporated in the mica assembly to improve the flexural and tensil characteristics. This construction is advantagous in handling the large size of the insulation, 2.4 x 3.5 m. The mica should be 1/10 mm thick for electrical reasons, but for reliability and handling a thickness of 1/4 or 1/5 mm may be needed. The overall thickness of the insulation assembly should be made as small as practical as this takes space that would be occupied by the copper conductor.

The inorganic materials alumina or its relative alumino-silicate are rigid ceramics in one common form. Both can be plasma sprayed in a thin layer onto a substrate which could be the stainless steel plates. The bond strength or adhesion is variable, but in this application bonding is probably a minimal problem. Little is known of the mechanical durability of sprayed ceramic coatings under very high compression. These ceramics are also available as a fibrous mat or paper, which can be impregnated or rigidized. The contiguous structure formed by the interlocking fobers reduces edge crumble and may make possible large area thin sheets which are manageable without any other backing. An alternative approach is to use a temporary mounting board for handling the insulator which can then be bonded to one plate turn.

Another form of alumina is an anodized coating formed on an aluminum surface. In general, durable coatings can be made; however, there are occasional imperfections or scratches on the coating which can redue the electrical resistance. Impregnating the anodized surface with a high radiation resistant organic polymer is a possible way to improve reliability. The bulk strength of the organic is not important because even if it depolymerized it would be fully contained.

There are some organic polymers with useable mechanical properties at $5\ 10^{10}$ rads, but

considering that organic impregnated fiber composites have a limited compressive load capacity (as experienced in the Bitter solenoid) these materials are not first order candidates for the *ITR* insulation.

The choice of insulator depends on the life cycle of the *TF* coil. If extensive, nonignited operation with H, preceeds D-T burning, after which limited ignited operation would be acceptable, an inorganically bonded insulator could be used.

Alternatively, if the *TF* coil can be disassembled and rebuilt in short order, either an organic insulator could be used and subsequently replaced, or a series of inorganic insulators could be initially used with a view to testing their fatigue life for subsequent use with D-T operations.

If extended ignited D-T operation were to predominate with little prior H plasma operation, no alternative to inorganic insulation exists.

At present no information on possible insulation indicates an unambiguous choice. The candidate materials and their probable lives are as follows:

1. Phlogopite mica bonded with inorganic materials including silicates and glass fiber. Fatigue life unlikely to exceed 20000 pulses but neutron irradiation to 10^{11} rads would not greatly affect its life.
2. Alumina, in the form of anodising or ceramic spray reinforced with glass fiber. Fatigue life unlikely to exceed 20000 cycles but neutron irradiation up to 10^{11} rads would not affect the life.
3. Glass fiber, mica, other inorganics bonded with polyimide resin. Fatigue life without irradiation could exceed 20000 cycles but irradiaiion of 10^{10} rads would terminate useful life.

In the absence of sufficient data on the insulators under the operating conditions of the *ITR*, testing of representative sample materials is absolutely necessary. Cyclic load compression tests are needed at various temperatures with at least some tests made after irradiaton, although this last requirement may be difficult to simulate accurately in the actual operating cycle. Some tests should

include insulaton compressed between plates which are tensioned simultaneously with the compression cycle. A few tests on prospective insulatons should be done according to accepted *ASTM* standards for comparison to othe well known materials.

Some specific considerations for testing are:

1. Resistance to thermal shock. ($77^{o}K$ - $293^{o}K$) The effects of thermal cycling to be determined during and after irradiation.
2. Samples should be water free -- i.e., dried. Water content must be controlled during fabrication and use to assure mechanical integrity at cryogenic temp.
3. The important properties to measure are:
   a - compressive strength
   b - dimensional stability
   c - flexural strength
   d - tensile strength
   e - electrical resistivity
   f - breakdown voltage
4. Electrical resistance to be tested under compression after the samples have been fatigued.
5. Measurement of progressive property degredaton during fatigue testing.

The insulation materials described here are certainly not the only choices. As different insulation properties are investigated for usefulness in the *ITR* some choices will probably be eliminated and new possibilities will appear.

A list of useful references on insulator properties is given in the next two pages.

Bibliography

Bauer and Bates, An Evaluation of Electrical Insulators for Fusion Reactors, BMI - 1830 (July 31, 1976)

W. W. Parkinson and O. Sisman, The Use of Plastics and Elastomers in Nuclear Radiation, Nucl. Eng. Design, 17, 247-280 (1971)

Proceedings of the Meeting on CTR Electrical Insulators, May 17-19, 1976, LASL, CONF-760558.

R. H. Kernohan et al., Low Temperature Radiation Effects on Organic Insulators, March, 1978.

F. W. Clinard, Jr., et al., Neutron Irradiation Damage in Al_2O_3 and Y_2O_3, LASL.

M. H. Van de Voorde, Effects of Radiation on Materials and Componenets, CERN 70-5, (Feb., 1970)

M. Van de Voorde, et al., Resistance of Organic and Inorganic Materials to High-Energy Radiation, CERN LABII-RA/PP/74-2 (June, 1974)

M. Van de Voorde, Mechanical Properties of Non-metallic Materials at 77 K in a Radiation Environment, CERN ISR-MA/72-14

V. A. J. Van Lint, et al., Effects of Ionizing Radiation on Electrical Properties of Refractory Insulators, CONF-750989-P2 (Mar., 1976)

Radiation Effects and Tritium Technology for Fusion Reactors, Vol. II (J. S. Watson, et al., eds.)

Muir and Bunch, High Energy Proton Simulation of 14 MeV Neutron Damage in Al_2O_3. In Watson reference preceding.)

Vook et al., Report to thh American Physical Society by the Study Group on Physics Problems Relating to Energy Technology: Radiation Effects on Materials, Rev. Mod. Phy., 47, Oct., 1975

J. R. Brown and N. M. Browne, Environmental Effects on the Mechanical Properties of High Performance Fibres (PBI, Nomex, Kevlar 49), Materials Research Labs, Maribyrnong, Australia, AD-A--032858, Aug., 1976 (ERA 02:045939)

J. Brewer and C. J. Cassidy, Changes in Mechanical Properties of Polyarylene (Stilan) and Polyimide (Kapton) Plastic Material Due to Gamma Radiation at Temperatures up to 500 F, ANL-CT-45824-0002 (June, 1975)

T. Brown an A. Tobin, Development of Large Insulator Rings for the TFTR, CONF-771029--152 (1977)

H. Brechna, Production of a Nuclear Radiation Resistant and Mechanically Tough Electrically Insulating Material, German (FRG) patent 1,719,241/B/, 27 Feb., 1975

C. J. McHargue and J. L. Scott, Material Requirements for Fusion Reactors, Metall Trans. A, Vol. 9A, pp. 151-159 (Feb., 1978)

American Society for Testing Materials, Book of ASTM Standards, Part 38, ASTM Standard D 257-76, D.C. Resistance or Conductivity of Insulation Materials, pp. 86-106 (1975)

Standard Recommended Practive for Exposure of Polymeric Materials to High Energy Radiation, Annu. Book ASTM Standards. 45, 528-532 (1975)

Standard Recommended Practice for Exposure of Adhesive Specimens to High Energy Radiation, Annu. Book ASTM Standards, 45, 537-541 (1975)

4.3 Stress, Thermal and Electrical Characteristics

These three characteristics are clearly tied together. Stresses and thermal characteristics determine the relative space devoted to steel and copper in the inner leg of the coil. The peak temperature in turn determines the electrical characteristics. The reference design point has been chosen to set the overall stresses in the inner leg at approximately 2.9 10^8 P (40 kpsi), and has chosen a copper to steel ratio of 2:1. Thus, the stresses are approximately 2.1 10^8 (30 kpsi) in the copper and 4.3 10^8 P (60 kpsi) in the steel. The hot-spot temperature in the copper is allowed to rise to 400 K at the end of the flat-top, including both ohmic and neutron-heating inputs. A power supply of 150 MW will drive the coil up in approximately 20 seconds and allow a flat top of approximately 20 seconds.

4.3.1 Stress Considerations

The coil is a bimetallic flat strip consisting of copper for electrical conductivity and high strength steel for structural integrity. Each turn is insulated on the faces by mica sheets. The general character of the coil may be seen in the radial plane view in Figure 4.3.1. The large radial thickness variation is evident in the sketch.

For purposes of stress analysis, each coil was assumed to be a closed ring. The analysis was conducted for the forces generated by a 10 T field at the position of the final plasma radius (see Table 2.1.1, for R_0 = 3.48 m). The magnetic forces were assumed to be considerably larger than the dead weight loads which were not included in the preliminary calculation.

The design constraints made apparent that the critical regions would be in the vicinity of the bore. The possibility for greater plate height with minimal field impact diminished the concern for stresses outboard of that zone. The region of primary interest appeared to be at the horizontal centerline near the bore. A minimum amount of material is available at that location to resist the force and moment acting across that section.

Next in order of concern would be the inner corners where the vertical forces at the horizontal centerline become transverse shear on the radial beams at the top and bottom of the plate together with a possible radial force from the radial outward loads on the outer vertical leg of the plate. This is a zone in which a joint would be required in the steel because of possible size restrictions in available plate stock.

A joint probably would be also required near the outer corner. However, the plate thickness is considerably greater there than at the inner corner. The cross section on the horizontal centerline is much stronger in that zone for the same reason.

The initial analysis consisted of determination of the vertical loads at the inner and outer edges using elementary beam theory with the assumption of simple supports at the ends. The local moment at the horizontal centerline was calculated by means of a simplified rigid frame analysis which also provided a more accurate value for the vertical forces. Finally, thick wall cylinder theory was employed to estimate the circumferential stresses near the bore due to the radial inward loads in that position. In this latter calculation, each of the 256 plates (or turns) was considered to be homogeneous and isotropic. This latter analysis also was supplemented by proportioning the computer results from *ALCATOR C*.

The results of the stress analysis appear in Table 4.3.1. The data are confined to the basic stresses in the critical zones. Additional analysis was made of a joint design at the inner corners. The numerical value of stress in Table 4.3.1 pertains to a weld in that location. A key and a multiple-pin configuration also were considered. A satisfactory design could be achieved with 2.5 cm diameter pins through overlapping steel plates. Local bearing stresses and possible rotation could arise with keys unless the mating edges were in near-perfect contact. Furthermore, keys with horizontal mating edges could not resist radial outward forces if any were to exist at that location. In addition, half the section would be removed for each side of the key so that the shear stresses above would be doubled. For pin connections the net section would be much closer to the gross section since the pins could be staggered thereby avoiding a large section loss at any specific position

along the beam.

In addition to the toroidal field in the cavity, there is a smaller vertical magnetic field through the coil that tends to cause a twisting in different directions of the upper and lower horizontal legs of the coil. On the assumption that the inward forces result in > 7.1 10^6 P (1000 psi) of normal pressure across the entire face on each side of the plate, the consequent frictional forces would be sufficient to counteract that torsional moment.

The coil has been presumed to be loaded to maximum field ~ 3000 times during the life of the magnet. If a factor of safety of 10 on life is used for evaluating the structural integrity, then the smooth-bar allowable stress would be of the order of approximately 3.6 10^8 P (51 kpsi) for the *OFHC* copper in the full hard condition according to the currently available data. If this stress is reduced to 2/3 of that value to account for imperfections, then the allowable stress would be 2.4 10^8 P (34 kpsi). This is based on uniaxial test data, of which there is not a large amount in the literature.

Analysis of notched fatigue strengths for a variety of the stronger steels indicate a safe working level of the order of 5.7 10^8 P (80 kpsi) for 40000 cycles at room temperature. Typical ultimate tensile stregnths would be in the 10 10^8 P (150 kpsi) range. Higher tensiles do not appear to result in higher low cycle fatigue strengths. A range of candidates includes 216, the Nitronics, 17-4 and 17-7 PH and Carpenter 18-18 plus. Some are heat treatable and some require cold working to achieve desired strengths.

In addtition to strength, thermal expansion behavior may be important. 17-4 and 17-7 have values of the order of 1. 10^{-5}/°C as compared to the copper value near 2. 10^{-5}/°C. This difference might lead to thermal stress problems when cooling the coils to LN_2 temperature.

It is concluded, by comparing the strength data with the theoretical stresses shown in Table 4.3.1, that the stresses are within the specifications.

4.3.1.1 Stress Analysis: Areas for Further Study

Based upon the results of the preliminary structural investigation, recommendations for further investigation would encompass the following topics:

1. A detailed stress analysis of the stresses and deformations at the throat of the magnet.
2. An accurate determination of stress intensity in the same region and an evaluation of the magnet structural integrity on the basis of fatigue as well as static stress.
3. Determination of acceptable imperfections, such as cracks, as a basis for final inspection procedures.
4. Analysis of thermal stresses due to nonuniform heating in the throat of the magnet and assessment of the factor of safety against buckling.
5. Design of the outer belt and determination of the required initial tension to assure satisfactory structural performance.
6. Determination of the impact of increasing the height of the plate to accommodate shear and radial tension forces at the joints near the corners.
7. Conduct of a tradeoff study among welding, pins, keys and other possible joining methods together with variations in plate depth to achieve the optimum solution.
8. Evaluation of the effect of fabrication dimensional tolerances on structural integrity.

Initially, the investigations would be performed analytically. There may be value in considering a program of verification testing to supplement the analysis. This would be important for delineation of reliable fatigue data on the copper and steel which would be appropriate candidates for the plate construction.

4.3.2 Thermal Considerations

The temperature distribution following a pulse is very nonuniform, with the peak temperature occurring at the mid-point of the inner leg where the current density is highest. In the reference design, the copper plates taper out to approximately the 1.2 m radius point and then are held at constant thickness. The steel continues to taper and occupies space not taken by copper or

insulation. The time evolution (in time steps of 1 s) of the temperature distribution of the *TF* coil is shown in Figure 4.3.2 in the case of only ohmic heating input. The *TF* coil has been divided into 35 segments, 15 of them in the throat, 10 in the straight legs and 10 in the outer edge of the coil. The temperatures of the segments are shown in Fig. 4.3.2. The lower numbers refer to segments in the throat.

The flat top is assumed to be terminated when the peak temperature in the *TF* coil reaches 400°K. The interturn steel is assumed to contribute to the heat capacity throughout the magnet. The 400°K point is reached after a flat-top pulse of 27 seconds. Figure 4.3.3 adds neutrons at a power level of 70 MW 2.5 s after the *TF* current reaches the flat top. In this case, the 400°K point is reached in 22 seconds. Figure 4.3.4 is considered an artificial case in which the heat capacity of the interturn steel is included only where the copper tapers, and not in the constant copper thickness regions of the magnet. This case was run to confirm the importance of intimate thermal connection in all regions of the magnet. The flat top is reduced to seven seconds, not by peak temperature but by the 150 MW power supply limit (see Figure 4.3.7).

Following a pulse the heat will diffuse and the plates will relax toward a uniform temperature. In the case represented by Fig. 4.3.3, that final temperature would be approximately 120°K, representing a deposition of 2.5 10^9 J of ohmic heating and 1.5 10^9 J of neutron heating into the 420 ton magnet. Recool to 77°K would require approximately 26000 liters of liquid nitrogen. The nitrogen would be supplied from a closed cycle refrigeration plant which would collect the vaporized gas.

Shorter pulse times will clearly result in smaller stored energy requirements, and in turn less dissipation of liquid nitrogen. For example, if the pulse were to be terminated after 10 seconds, the ohmic dissipation would be 1. 10^9 J and the neutron deposition 0.5 10^9 J. The recool nitrogen requirements would drop to approximately 10000 liters.

4.3.3 Electrical Characteristics

The reference design magnet is assumed to have 256 turns, requiring a series current of 250

kA. Assuming a peak power capability of 150 MW, the peak voltage would be 600 volts. This is matched to the peak power but not the impedance of the present transformer/rectifier unit at Garching. It is not feasible to build Bitter magnets at appreciably lower current levels and therefore a new, or possibly rebuilt transformer/rectifier unit seems necessary.

The power versus time curves for the three thermal cases presented in Figures 4.3.2 - 4.3.4 are given in Figures 4.3.5, 4.3.6, and 4.3.7. The flat top is held until a peak temperature of 400 K is reached. In the case of Figure 4.5 (ohmic heating alone), and Figure 4.6 (ohmic plus neutrons), the 400 K condition results in flat top pulses very much longer than realistic under the 1.5 10^9 J limitation of the present rotating equipment at Garching. Table 4.3.2 summarized the electrical characteristics of the reference design.

TABLE 4.2.1

High-Strength, High-Conductivity Materials for High-Performance Electromagnets:

	Alloy Name	Copper Development Association Number	Producers	Trade Name	Room Temperature Electrical Conductivity (% IACS)
1.	Cryogenic-Grade Oxygen-Free-Electronic Copper (OFE Copper)	CDA 101	Phelps-Dodge and AMAX	PDOF OFHC	101% to 102%
2a.	Oxygen-Free-Copper	CDA 105	Phelps-Dodge and		100% to 101%
2b.	with Silver (OFS Copper)	CDA 106	AMAX		
2c.		CDA 107			
3a.	0.2% Alumina Copper		Glidden Metals	GlidCop AL-10	92%
3b.	0.4% Alumina Copper		Glidden Metals	GlidCop AL-20	89.5%
3c.	0.7% Alumina Copper		Glidden Metals	GlidCop AL-35	85%
3d.	1.1% Alumina Copper		Glidden Metals	GlidCop AL-60	78%
4.	Beryllia-Copper		Handy and Harman	Cubaloy	≈90%
5.	Cadmium-Oxide Copper		Handy and Harman		≈90%
6.	Silver-Oxide Copper		Handy and Harman		≈90%
7.	Zirconia-Copper		Raytheon and Revere Copper and Brass (Rome, New York)		≈90%
8a.	Cadmium-Copper	CDA 162	Mallory and several others		80%
8b.		CDA 164			to
8c.		CDA 165			97%

Table 4.2.1 (cont.)

Alloy Name	Copper Development Association Number	Producers	Trade Name	Room Temperature Electrical Conductivity (% IACS)
9. Cadmium-Chromium Copper		Phelps-Dodge	PD-135	
10a. Chromium-Copper	CDA 182	AMAX and Mallory and others	AMCHROM	80% to 85%
10b.	CDA 184			
10c.	CDA 185			
11. Zirconium-Copper	CDA 150	AMAX	Amziro	90% to 95%
12. Zirconium-Chromium Copper		Eltek	Elbrodur	81% to 90%
13. Magnesium-Phosphorus-Copper	CDA 155	Hussey Metals Company Copper Range Company	SSC-155	70% to 90%
14. Magnesium-Zirconium-Copper		AMAX	MZ Copper	≈90%
15. Magnesium-Zirconium-Chromium Copper		AMAX	MZC-Copper	80%
16. Silver-Copper		Army Signal Corps Army Signal Corps Handy and Harman G. Frommeyer and G. Wasserman	 Consil 6	84.6% to 89.4% 71.9% to 73.5% 71.9, 73.5 70% to 75%

Table 4.2.1 (cont.)

	Alloy Name	Copper Development Association Number	Producers	Trade Name	Room Temperature Electrical Conductivity (% IACS)
17a.	0.5% Beryllium-Copper	CDA 175	Brush Beryllium and Berylco	Brush 10	48% to 60%
17b.				Brush 50	48% to 60%
17c.	2.0% Beryllium-Copper	CDA 170		Brush 25	20% to 28%
17d.		CDA 172		Brush 190	20% to 28%
18a.	Niobium-Copper		Harvard University		
18b.					60% to 85%
18c.					
19.	Tungsten		AMAX Specialty Metals, Schwarzkoff Dev. Corp., Fansteel, and others		31%

TABLE 4.2.2

Sample Orientation	Yield Strength (0.5% Strain) in Psi	Ultimate Tensile Strength in Psi	Elongation to Fracture in Percent
Room Temperature Tests:			
Longitudinal	46,061	46,536	21.75
Longitudinal	45,862	46,219	21.75
Average:	45,961	46,377	21.75
	± 140	± 224	---
Transverse	48,598	48,598	16.50
Transverse	48,306	48,306	16.50
Average:	48,452	48,452	16.50
	± 207	± 207	---
Liquid-Nitrogen-Temperature (77 K) Tests:			
Longitudinal	49,606	51,510	20.88
Longitudinal	49,685	51,987	21.88
Average:	49,645	51,748	21.38
	± 56	± 337	±0.71
Transverse	51,938	52,136	18.25
	52,755	53,072	18.12
Average:	52,347	52,604	18.19
	± 578	± 662	±0.09

TABLE 4.2.3

Results of Tensile Tests on Carpenter Technology 18 - 18 Plus Stainless Steel:

All eleven tensile test specimens were 0.070" thick, with a gage section 0.500" wide and 2.0" long. Eight samples (A1, A2, A3, B1, B2, B3, D1, and D2) were prepared from 67% cold-worked material. Three samples (C1, C2, and C3) were prepared from annealed material. Two of these samples (C2 and C3) broke near the grips rather than in the gage section; consequently, no elongation-to-fracture values are included, and the values of yield strength and ultimate tensile strength are only lower bounds to the true values. The cross-head speed used in the tests was 0.05" per minute.

Sample Number	Yield Strength in psi	Ultimate Tensile Strength in psi	Elongation to Fracture in Percent
A1	225,965	234,290	14.00
B1	222,185	233,378	13.55
D1	215,538	229,972	13.50
Average	221,229	232,547	13.68
	±5,279	±2,276	±0.28
C1	80,791	132,592	83.75
Liquid-Nitrogen-Temperature (77 K) Tests:			
A2	314,286	376,905	14.95
A3	328,357	376,835	14.975
B2	339,645	375,284	14.95
B3	336,552	373,348	14.00
D2	347,894	376,488	15.575
Average	333,347	375,772	14.89
	±12,745	±1,503	±0.56
C2	>155,058	>255,669	-----
C3	>106,749	>259,787	-----
Average	>130,904	>257,728	
	±34,160	±2,913	

TABLE 4.2.4

Compressive Load	~ 200 MP (30 kpsi)
Fatigue Life	20000 cycles
Attenuated Neutron Fluence	10^{20}n cm^{-2} (10^{11}rad)
Operating Temperature (under loading)	77 to 300 K in 20 sec.
Desired Maximum sheet size	2.4 × 3.6 m
Dielectric Strength	~ 5 V per turn
Maximum Desired Thickness	0.5 mm

TABLE 4.3.1

PLATE STRESSES

Location and Type	Magnitude, 1000 psi	
Horizontal Centerline near Bore,	Copper	Steel
Bending plus Tension	33	66
Near Midspan of Radial Beams,		
Bending plus Tension	35	70
Horizontal Centerline near OD,		
Bending plus Tension	8	16
Inner Corners,		
Shear alone	15	30
Maximum Shear (Shear Combined with Tension)	17	34
Horizontal Centerline Zone near Bore,		
Normal Pressure on Plate Faces	≤ 20	≤ 20

Note: Allowable stresses for shear are usually 60 percent of the allowable stresses for normal loads.

TABLE 4.3.2

SUMMARY OF ELECTRICAL CHARACTERISTICS

TF field at R_f = 1.27	10 T
Peak Power	150 MW
Peak Voltage	600 v
Peak Current	250 kA
Inductive Engergy	1.2×10^9 joules
Flat-top time with ignited plasma	22 seconds
Total resistive energy at end of flat top	2.5×10^9 joules

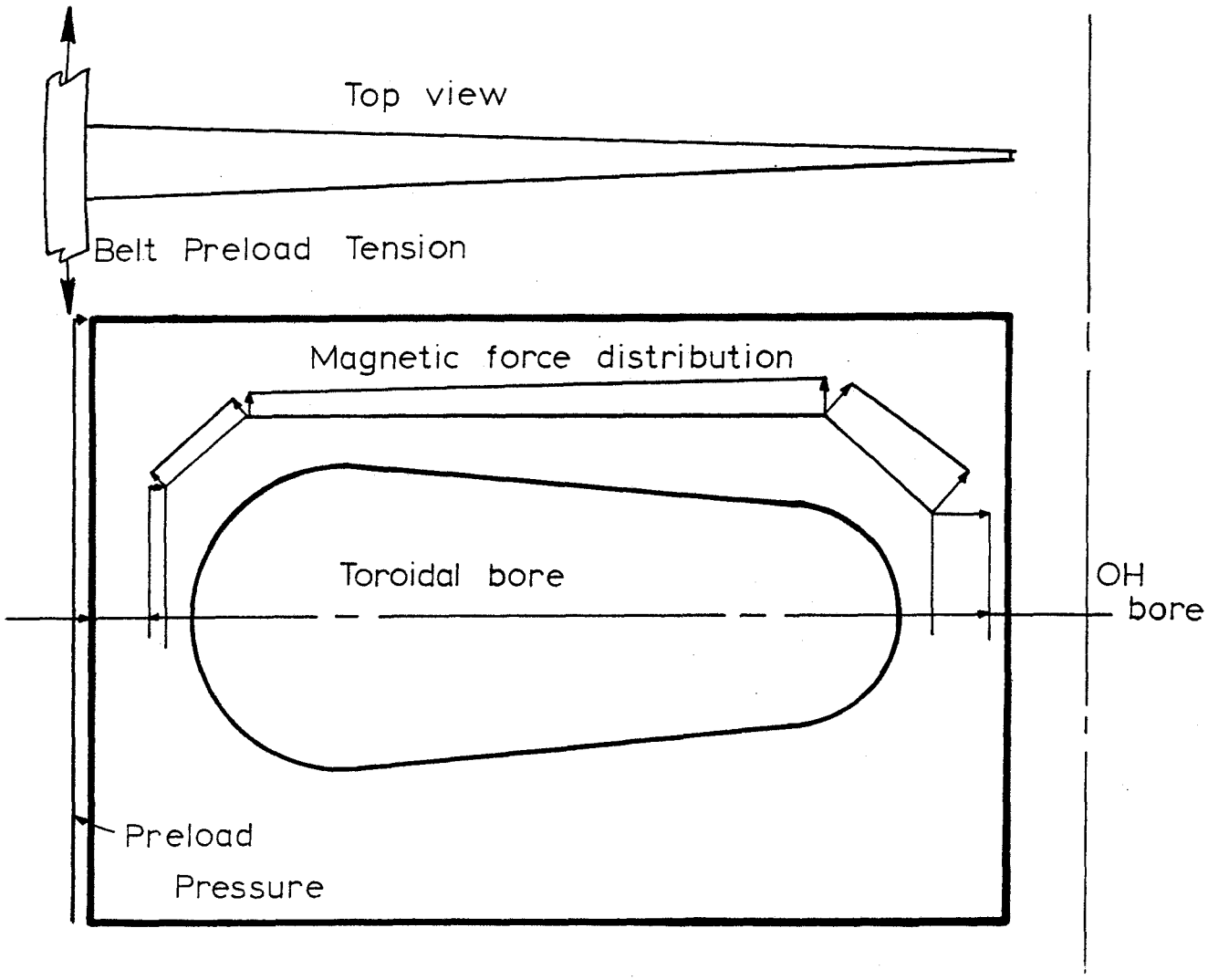

Figure 4.3.1 Sketch of Plate Simulating Coil Structure for Stress Analysis Under Magnetic Forces.

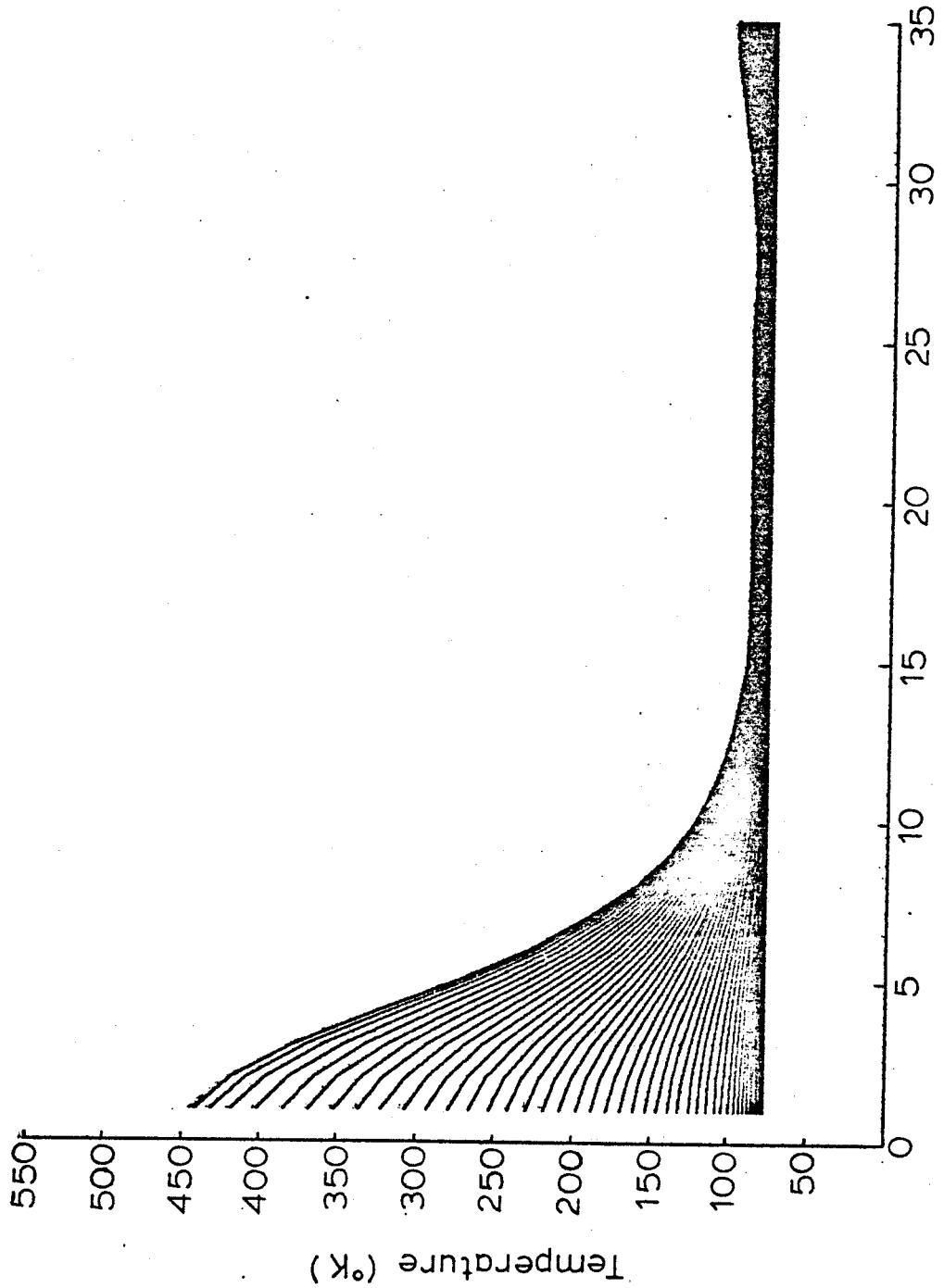

Figure 4.3.2 Temperature of segments of TF coil. Ohmic power only; low numbers correspond to throat region.

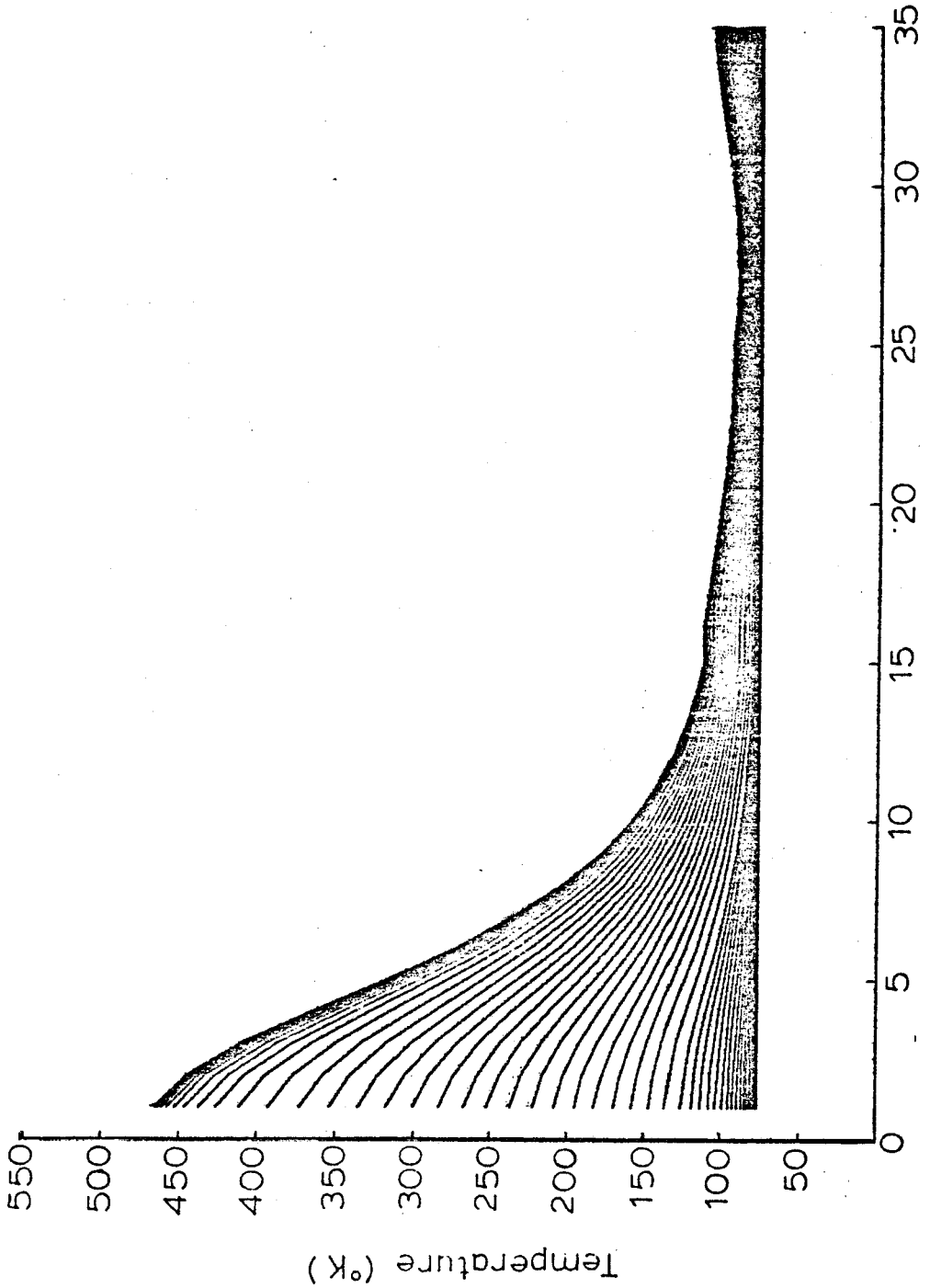

Figure 4.3.3 Same as Figure 4.3.2, but including both ohmic and neutron power.

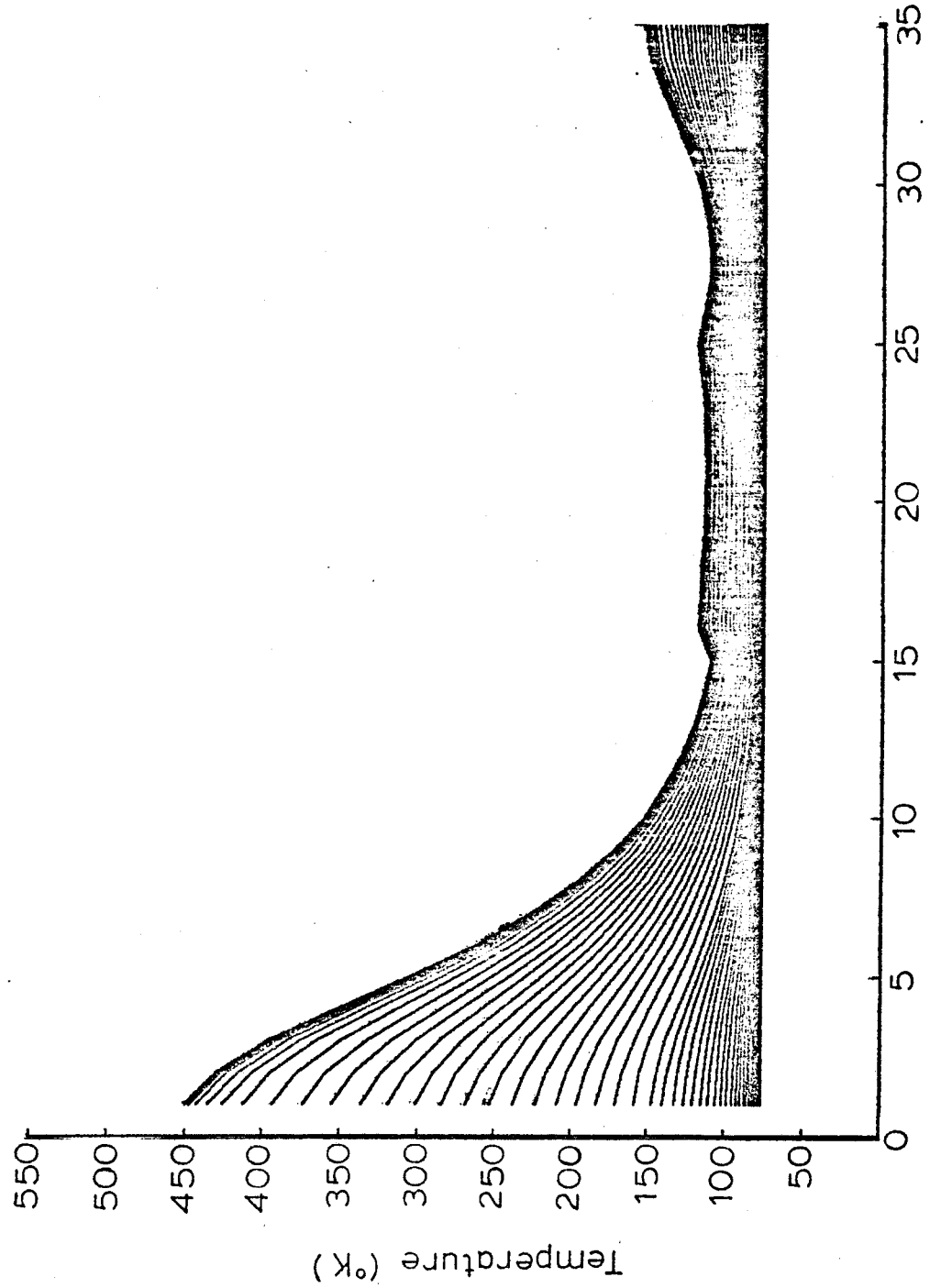

Figure 4.3.4 Same as Figure 4.3.3, but steel reinforcement does not carry the heat for $R > R_f$.

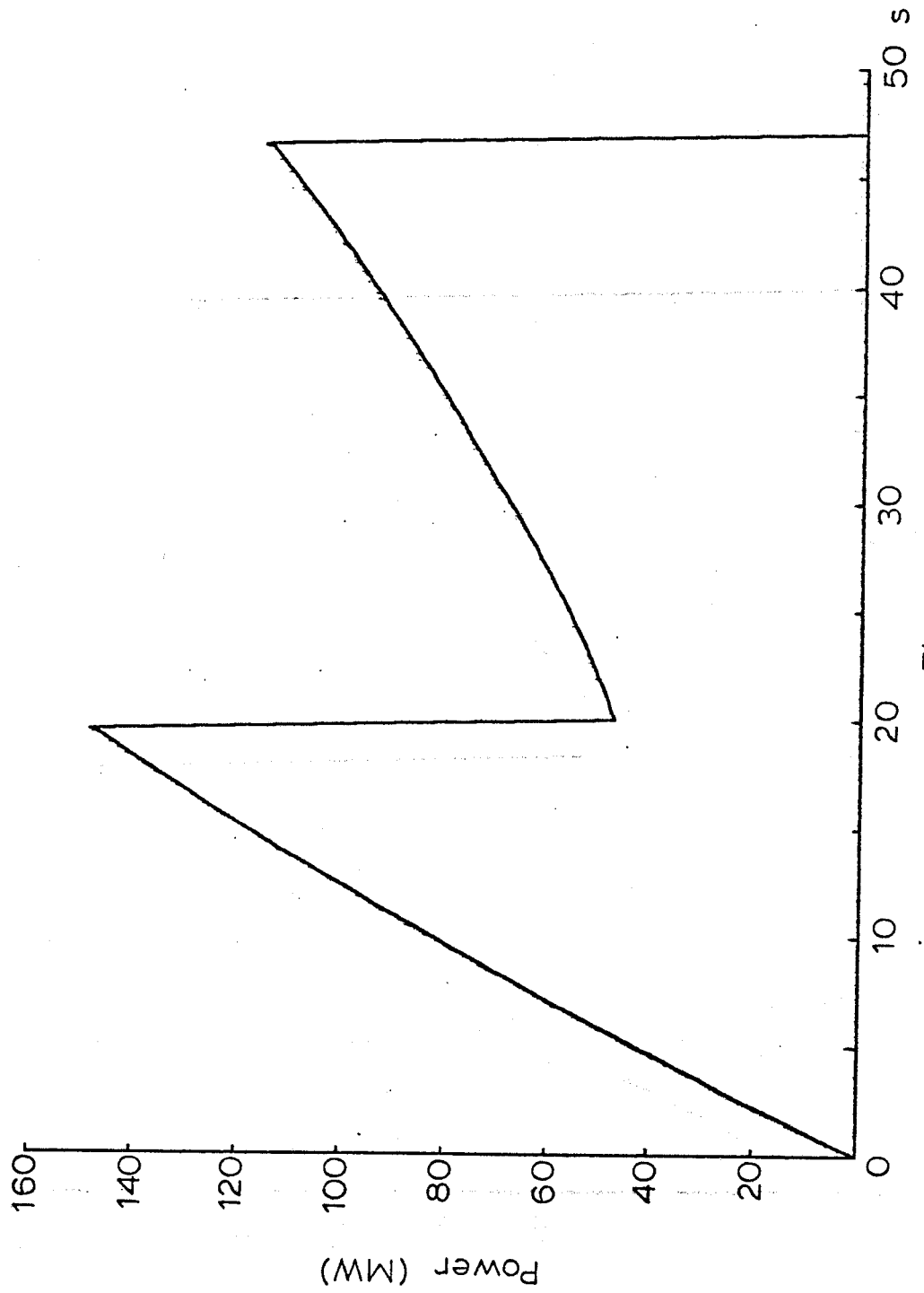

Figure 4.3.5 Power vs time for the case of Figure 4.3.2.

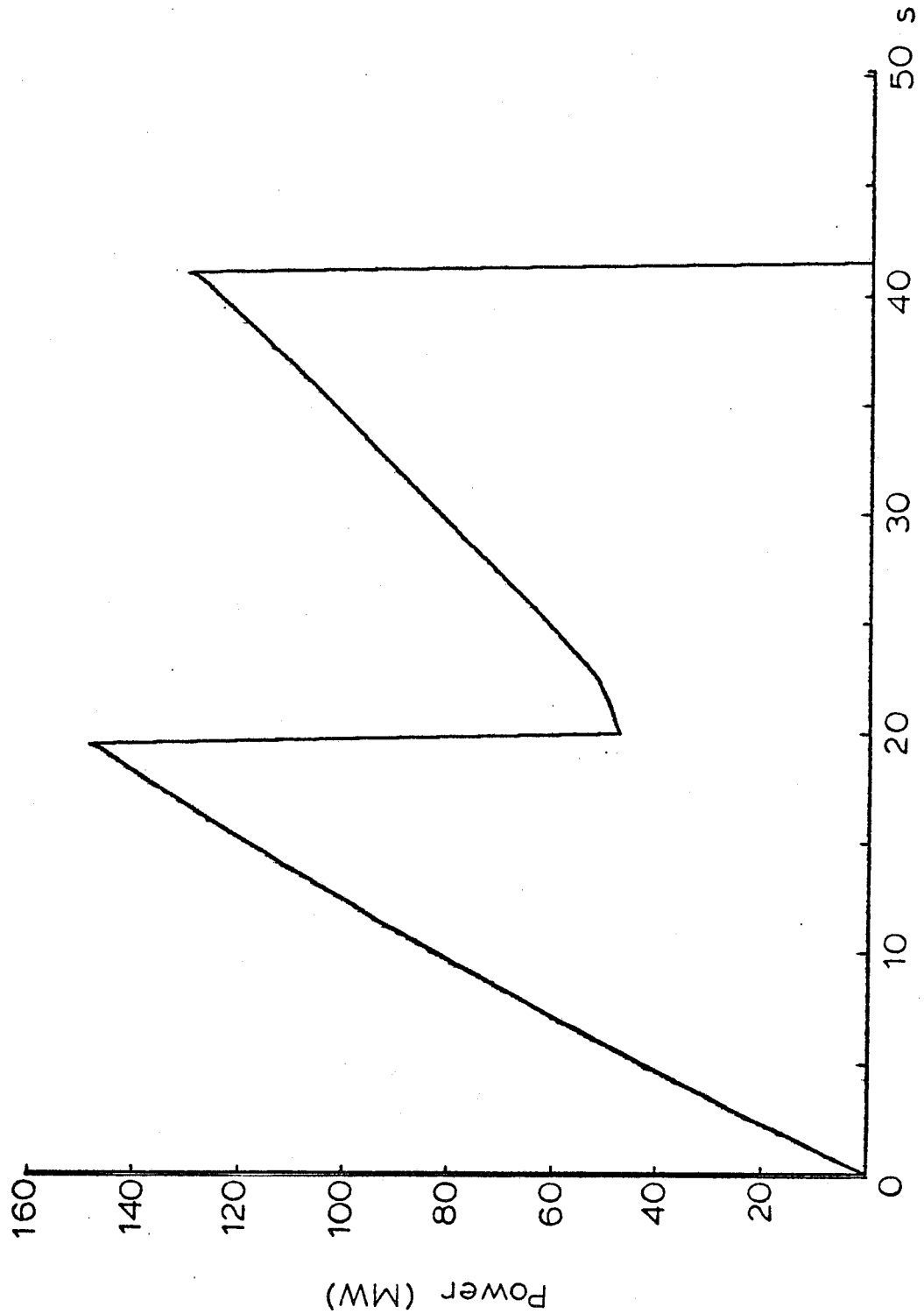

Figure 4.3.6 Power vs time for the case of Figure 4.3.3.

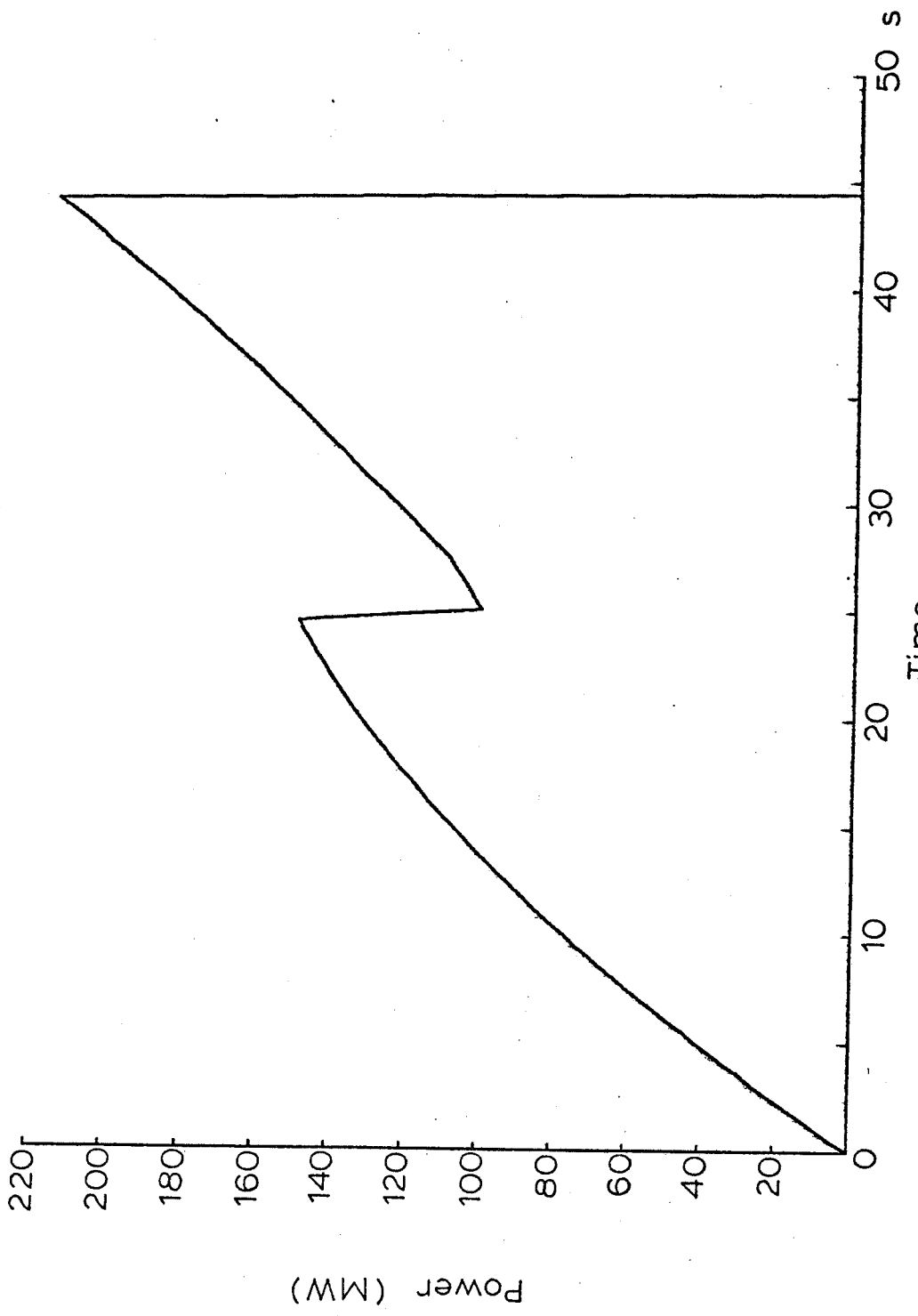

Figure 4.3.7 Power vs time for the case of Figure 4.3.4.

5.0 Toroidal Field Coil Fabrication

5.1 Individual Turn Construction

The *TF* coil reference design calls for 256 turns, each turn consisting of a single piece copper plate, a steel reinforcing plate made up from four subsized pieces, and an insulation plate, made up from mica bonded between thin protective aluminum or steel sheets. The steel and copper pieces are appropriately interlocked in order to assure equal strains. In addition to the interlocking, preclamping from external bands plus magnetic clamping add a face pressure which supplies a friction bond.

The copper sheets are considered to be available in single size sheets, but the steel is not and must be made up from interlocking sub-sized pieces. Figure 5.1.1 is illustrative of a possible build-up. The steel in the inner leg would be of the highest quality, whereas the top, bottom and outer pieces, being thicker than required, might use steel of reduced strength.

The construction in Figure 5.1.1 is intended to be illustrative only. It is unlikely that those joint details would be satisfactory and pinned joints or welded joints would need careful investigation (see section 4.3.1).

In the construction of Figure 5.1.1, the copper tapers to a radius of only 1.3 m from the major axis; beyond that it is held to a constant thickness of 0.75 inch. The copper is held to constant thickness for three reasons:

(1) The resistance of the outer part of the magnet is ~ 0.5 of the total resistance at the end of the pulse (from calculations shown in section 4.3.2). Increasing the amount of copper here would only marginally decrease the peak power at the end of the pulse, and the total ohmic energy dissipated in the magnet.

(2) The copper remains in a thickness range suitable for cold working without resorting to a laminated turn build-up.

(3) The magnet becomes increasingly porous to compression field which can readily penetrate

through the interturn steel. This reduces the local variation of vertical field at the plasma to less than 5% (see section 2.2).

5.2 Injection Port Construction

It is proposed that the 256 turns of the magnet be uniformly distributed, but that turns be locally perturbed around eight 0.45 m square horizontal injection ports. These ports would be centered in each of eight sub-units of the coil (see section 5.3). More modest vertical access for diagnostics would presumably be incorporated into the eight split flanges flanking the eight sectors.

The port concept is illustrated in Figure 5.2.1 and Figure 5.2.2. The three turns on each side of the horizontal opening are "bent" as illustrated. The reduced turn thickness and resultant higher current density compensates to a large degree for the opening. While the turn thickness is reduced, the copper thickness actually remains constant as the steel is appropriately reduced. The bending and shear stresses at the "bends" in the steel plates, particularly those adjacent to the port, would be too large without additional support. However, such a support is easily supplied by short beams near the top and bottom of the port plates, clamped together with vertical bars. The "bent" plates would be extended in the radial direction near the top and bottom of the plates, while the beams would be extended in the toroidal direction so that the vertical bars clear the port.

The ripple has not been calculated for this reference port, but similar designs being considered for an *ALCATOR C* Up-Grade yield ripples of a few percent at the limiter edge.

5.3 Magnet Assembly, Disassembly, and Remote Maintenance

5.3.1 Introduction

The overall magnet assembly is patterned after *ALCATOR C* in order that the practical experience obtained in the construction of that machine can be carried over into the construction of this larger reactor. The only changes in the general arrangement are those made necessary by the increased size or by the requirement that the reactor be designed for remote disassembly.

The work now has the status of a conceptual design just prior to the first layout drafting. It consists of word descriptions plus a few sketches.

The necessary reactor design changes and the equipment required for remote maintenance are recognized in the process of writing the procedure for the assembly. The assembly procedure makes up the greater part of this chapter. The disassembly procedure is visualized as being the reverse of the assembly process.

The basic criteria for the design and for the selection of remote maintenance equipment is the requirement that a repair or modification shall take place in some reasonable period of time, approximately thirty to sixty days. Since experience with *ALCATOR A* indicates that the failure of a coil or a vacuum vessel wall is a very unlikely event, spare replacement modules will be built and no provision is to be made for remotely restacking radioactive Bitter plates or replacing a bellows. This greatly simplifies the hot cell tooling.

It is assumed that the initial assembly will be a hands-on operation. However, some portion of this assembly should be done with the remote handling equipment to verify its later use and to establish realistic procedures and time estimating.

5.3.2 Conceptual Design

The general arrangement of the magnet system will be the same as *ALCATOR C* which is shown in Figure 5.3.1. The magnet system consists of five major parts: the toroid of Bitter plates,

the upper poloidal and lower poloidal field structures, the *OH* field central coil, and the fiberglass thermal barrier.

The toroid of Bitter plates is the basic structure. It is supported by three equally spaced A-frame legs at a height above the floor which will permit the bottom half of the fiberglass thermal barrier to be lowered down so that it can be moved out between the legs. The toroid of Bitter plates is solidified into a solid structure by two circumferential fiberglass bands and the associated clamps which press all the wedge shaped plates toward the center. The two bands are supported at three points around the circumference by three fiberglass plates attached to th

The upper and lower poloidal field structures are each independent assemblies formed by the coils and their supporting frame. Each can be moved away from the toroid as a unit.

The central *OH* field coil is an independent unit which can be lifted out of the toroid bore.

The three piece fiberglass thermal barrier surrounds all of the other parts. All the coils are cooled by flooding their upper surfaces with liquid nitrogen. The excess flows off and is collected in the bottom of the fiberglass thermal barrier and is recirculated.

The Bitter plate toroid for *HFITR* is made up of eight loosely stacked modules of Bitter plates. Each module of plates along with a 45^0 sector of vacuum vessel is held together by its own assembly table until the fiberglass bands and clamps pull them together into a solid structure. The flanges at each end of the sector of the vacuum chamber have approximately the same external dimensions as the Bitter magnet plates and are sandwiched between the magnet plates when the modules are assembled. Seam welds around the outer edges of the mating flanges seal the vacuum vessel.

The magnet is divided into eight individual modules. The Bitter plate stacks and bellows are identical so that a spare unit can be placed anywhere in the toroid. This is feasible since the only difference between modules will be the flanges which accept the diagnostic instrumentation and provision will be made for the hands-off replacement of these flanges.

The reactor is located in a high bay area which is equipped with an overhead crane of sufficient capacity to lift the *OH* field central coil or the upper poloidal field structure. The individual modules will not be lifted by the overhead crane.

Off to one side of the reactor high bay area is a hot cell which is equipped with manipulators and special tools to permit some repairs on a module.

Each module when not clamped into the toroid is supported on a wheeled assembly table so that the module can be moved from its proper position in the toroid into the hot cell. The tracks on which the module moves are arranged as proposed for the *HFCTR* reactor shown in Figure 5.3.2 for general information. The circumferential tracks serve also to guide the shielded mobile floor unit shown in Figure 5.3.3. This unit along with a shielded crane cab, Figure 5.3.4, contains manipulators which will be used to disconnect all leads and connections to the toroid and to loosen the clamps on the tension band so that an individual module can be removed from the complete toroid.

5.3.3. Assembly of the Individual Modules

1. Attach the vessel bellows to the neutral beam port flange.
    a. Using the overhead crane with a sling attached to the neutral beam port flange, move the neutral beam port flange into position on the assembly table.
    b. Attach a sling to the vessel bellows sections and move the bellow onto the assembly table adjacent to the neutral beam port flange.
    c. While still attached to the overhead crane, move the bellows into proper relation to the neutral beam port flange and clamp the two pieces together.
    d. Tack-weld the vessel bellows to the neutral beam port falnge and then remove the clamps.
    f. Clean the weld and test it for acceptability.
    g. Repeat steps C-1-b through C-1-f to attach the other half of vessel bellows to the neutral beam port flange.
2. Install instrumentation to the vessel bellows (i.e., thermocouples, etc.)

3. Attach insulation to the vessel bellows and to the faces of the neutral beam port flange.
4. (See note) Stack the Bitter pates over one-half of the vessel bellows.
    a. Starting at the face of the neutral beam port flange, while using the overhead crane attached by a sling to an individual Bitter coil plate, thread the first Bitter plate over the vessel bellows.

        NOTE: The Bitter plates which are located nearest to the neutral beam port have a built-in off-set which straddles the neutral beam port. Care must be taken to use the proper Bitter plates and to position them correctly in respect to the neutral beam port flange.

    b. Clamp or clip the Bitter plate, insulation and flange together.
    c. Repeat steps C-4-a and C-4-b until all the Bitter pates for one-half the module are properly positioned and clamped.
5. Attach the split flange to the end of the vessel bellow.
    a. Using the overhead crane with an appropriate sling, move the split flange into position over the vessel bellows, adjacent to the last Bitter plate.
    b. Fixture the split flange to the vessel bellows and tack-weld the two together.
    c. Remove the holding fixture and completely weld the split flange to the vessel bellows.
    d. Clean the weld and test it for acceptabilty.
6. Complete the second half of the module by repeating steps C-4 and C-5.

5.3.4. Placement of Tension Ring Below the Radial Spur Tracks

1. Lift the rail sections on the radial spur tracks.
2. Using the overhead crane position the lower tension ring into the recess below the radial spur tracks.
3. Replace the rail sections over the tension ring.

5.3.5. Combining the Modules to Form a Torus

1. Move the individual module on its assembly table along the hot cell track until it meets the

circumferential track.

2. Lower the tapered circumferential track rollers of the assembly table onto the circumferential track and retract the straight track rollers.
3. Move the assembly table with its module around the circumferential track until it reaches the intersection of the radial spur track for its position in the torus.
4. Lower the assembly table straight track rollers onto the radial spur tracks and retract the tapered circumferential rollers.
5. Move the assembly table inwardly along the radial spur track until it reaches its stop point.
6. Secure or lock the assembly table to the floor so that the unit does not move.
7. After each individual module has been assembled as per steps C-1 through C-6, perform steps E-1 through E-6 to move all the modules together for final assembly.
8. Lock the 8 assembly tables together.

5.3.6. Assembly of the Toroidal Magnet

1. Weld the module sectors together.
    a. Tack-weld the 8 individual modules to their adjacent modules at the split flanges.
    b. Completely weld the split flanges together for the eight modules.
    c. Clean the welds and test for weld acceptability.
2. Position the lower tension ring.
    a. Lift and remove the rail sections from over the lower tension ring.
    b. Using the overhead crane with the special lifting fixtures, lift the lower tension ring and position it at the proper height for clamping.
    c. While supporting the lower tension ring with the crane, position the individual clamps and slightly tighten the bolts, to secure the clamp ring. (There will be numerous clamps with approximately 6 bolts for each clamp.)
    d. Release and remove the lifting fixture from the lower tension ring.
3. Position the upper tension ring.
    a. Using the overhead crane and the special lifting fixture, lift and position the upper

tension ring.

b. While supporting the upper tension ring with the crane, position the individual clamps and slightly tighten the bolts to secure the clamps for the upper tension ring.

c. Release and remove the special lifting fixture.

4. Using the shielded mobile floor unit and a prearranged clamp tightening sequence, fully tighten the clamps for both the upper and lower tension ring.

5. Install the permanent "A" frame supports.

a. Raise the assembly tables together a few inches so that they are at the proper height to install the permanent "A" frame leg supports.

b. Disengage the locks of the assembly table located nearest to the rail spur which connects the hot cell to the circumferential track from the two adjacent assembly tables.

c. Lower the unlocked assembly table a few inches to clear the bottom of the module and unlock the table from the floor.

d. Move the assembly table radially outward on the spur radial track, until it passes over the circumferential track and continue to move it along the spur out of the area.

e. Disengage the assembly table located on the opposite side of the main spur in direct line with the table which was just removed.

f. Repeat steps F-5-c and F-5-d to move the second assembly tables under the bottom of the Bitter coils along the one main rail spur leading to the hot cell area.

g. Install the first "A" frame leg support in the location nearest to the second assembly table which was just removed.

h. Disengage the assembly table located just counter-clockwise to the "A" frame leg from its adjacent assembly table.

i. Lower the unlocked assembly table a few inches until it clears the bottom of the module it was supporting and unlock the table from the floor.

j. Move the assembly table radially outward on its radial spur track until it reaches the

circumferential track.

k. Lower the tapered circumferential track rollers of the assembly table onto the circumferential tracks and retract the straight track rollers.

l. Move the assembly table around the circumferential track until it reaches the spur leading out of the area.

m. Lower the assembly table straight track rollers onto the spur track and retract the tapered circumferential track rollers.

n. Move the assembly table along the spur track out of the area.

o. Repeat steps F-5-h through F-5-n to remove the two assembly tables located counter-clockwise to the assembly table which was just removed.

p. Install the second "A" frame leg support at a location 120° counter-clockwise to the first "A" frame leg support.

q. Repeat steps F-5-h through F-5-n to remove the three remaining assembly tables. These tables will be moved clockwise along the circumferential track.

r. Install the third "A" frame leg support.

5.3.7. Installation of the Poloidal Field Coils

1. Place the lower poloidal field coil onto its transfer dolly and move the dolly into position under the Bitter coil. (There is one radial spur track which connects to the spur track leading out of the area and which continues straight through under the complete device.)
2. Raise the dolly support platform with the poloidal field coil up until it is positioned at the proper height for the vertical side supports.
3. Attach the overhead crane to the upper poloidal field coils assembly and carefully lower it over the top of the Bitter coils with the side vertical support bars straddling the outside of the device.
4. Attach the bolts through the side vertical support bars which assemble the upper and lower poloidal field coils to each other and to the sides of the tokamak.
5. Connect the power supply lines for each individual upper and lower coil. (If these lines

interfere with the positioning of the central *OH* field coil installation, delay the step until after the *OH* coil is positioned.)

6. Lower the dolly support platform away from the lower poloidal field coil and move the dolly out from under the device between the "A" frame support legs.

5.3.8. Installation of the *OH* Field Central Coil

1. Connect the overhead crane to the lifting device on the *OH* field central coil.
2. Lift the assembled *OH* field coil and carefully position it in the center of the upper poloidal field coils.
3. Disconnect and remove the lifting device.
4. Using the shielded crane cab, attach the bolts which lock the *OH* field coil in place.
5. Connect the power supply lines for the *OH* field coil.

5.3.9. Installation of the Fiberglass Thermal Barrier

1. Using the overhead crane, place the lower cylindrical fiberglass thermal barrier onto the transfer dolly (same dolly which was used to transfer the lower poloidal field coils).
2. Move the dolly on its spur tracks under the lower poloidal field coil assembly.
3. Raise the platform so that the fiberglass thermal barrier is lifted and positioned around the lower portion of the device.
4. Using the overhead crane, lift the upper cylindrical portion of the fiberglass thermal barrier and lower it over the upper portion of the device.
5. Secure the upper and lower thermal barriers together.
6. Release the crane from the upper thermal barriers and use it to lift and position the thermal barrier cover plate onto the top of the device.
7. Secure the thermal barrier cover plate to the upper thermal barrier.
8. Lower the dolly platform and move the dolly out from between the "A" frame support legs.
9. Connect the required diagnostic instrumentation through the openings in the thermal barrier.

5.3.10. Installation of the Neutral Beam Injectors

1. Move the neutral beam injector which is supported on its own vehicle along the main spur tracks until it meets the circumferential track.
2. Lower the tapered circumferential track rollers onto the track and raise the straight track rollers.
3. Move the neutral beam injector around until it reaches the radial location for the module it is to be connected to.
4. Lower the straight track rollers and raise the tapered circumferential track rollers.
5. Move the neutral beam injector radially inward until the flange of the neutral beam meets the module neutral beam port flange.
6. Lock the vehicle in position onto the floor.
7. Connect the flanges together.
8. Connect the various utility quick connect joints together.
9. Repeat steps J-1 through J-8 for the other five neutral beam injector.
10. Place a cover plate over the neutral beam ports which do not have neutral beam injectors.

List of Major Items of Assembly Equipment

Assembly of Individual Modules in Non-Radioactive Area

1. Two-ton overhead crane.
2. Module assembly talbe, wheeled.

Assembly of the Toroidal Magnet in a Radioactive Area

1. Tracks in the floor to guide the assembly tables.
2. Shielded cab crane with manipulators.
3. Tension ring lifting fixture.
4. Tool for tightening six nuts on clamps.
5. Shielded mobile floor unit with manipulators.
6. "A" frame leg sling.

7. Lower poloidal field coil transfer dolly.
8. *OH* Coil lifting sling.
9. Automatic welder for split flanges.

Disassembly of the Toroidal Magnet

(As for assembly but add)

1. Automatic weld cutting machine.

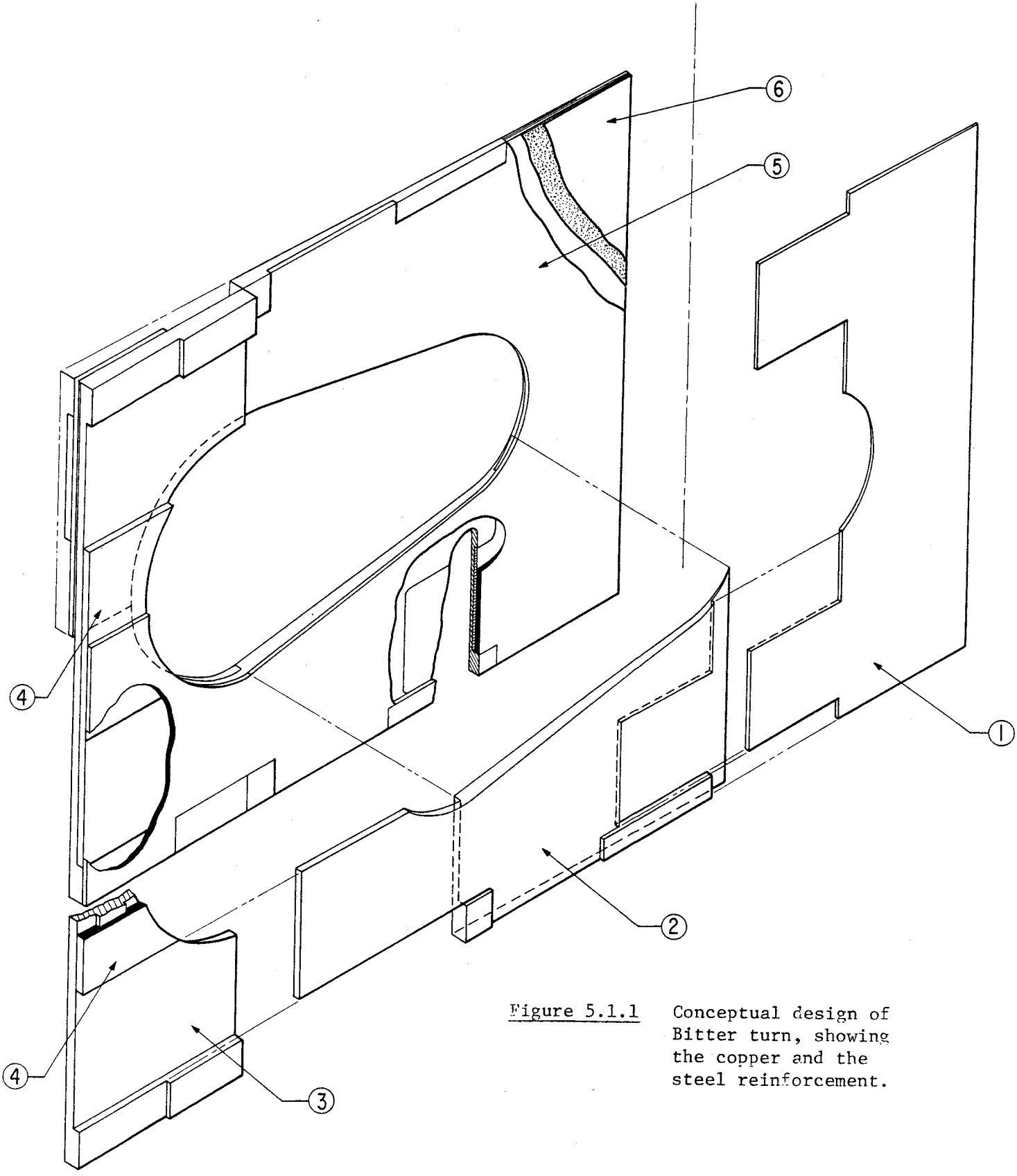

Figure 5.1.1 Conceptual design of Bitter turn, showing the copper and the steel reinforcement.

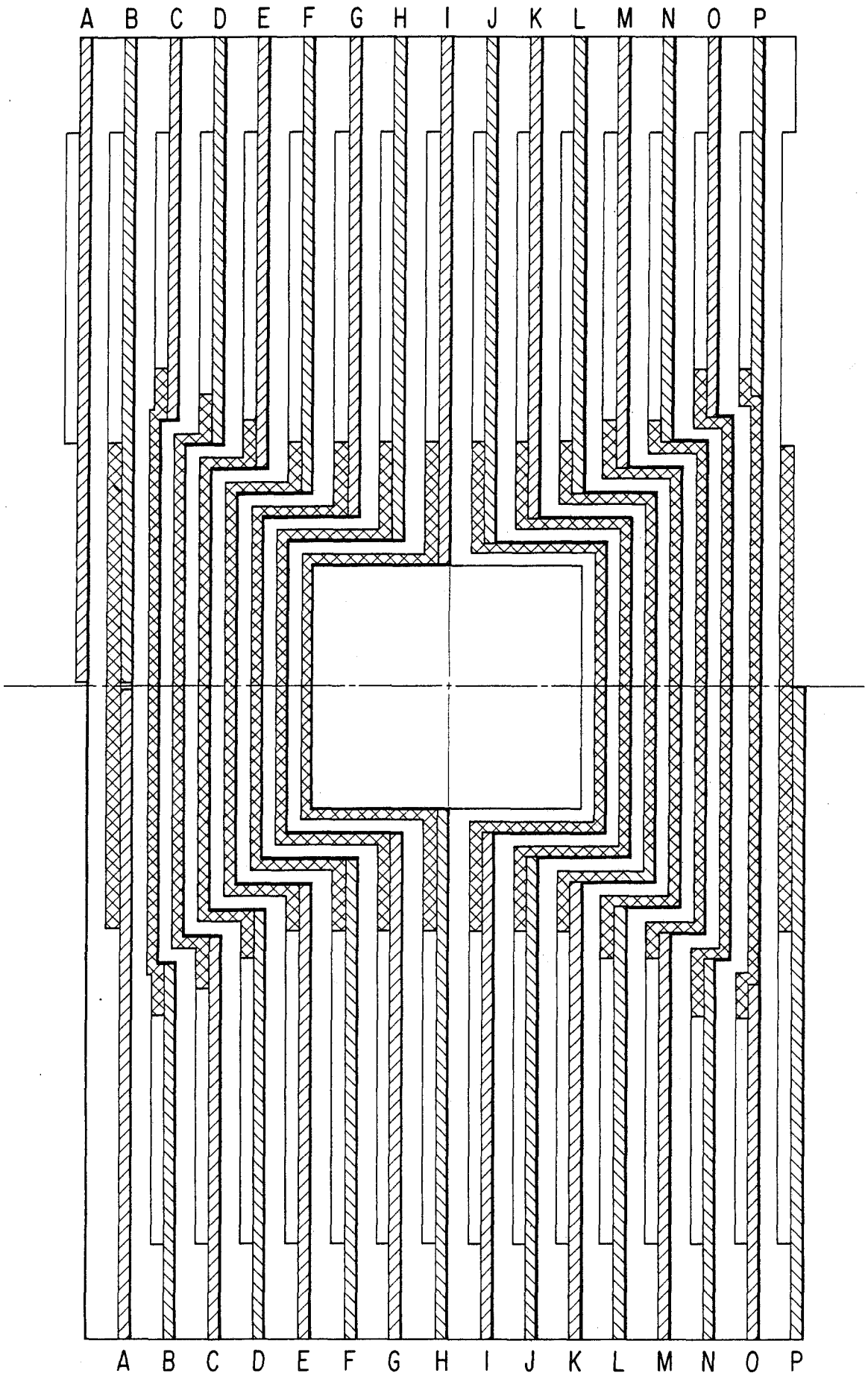

Figure 5.2.1 Port design. Radial view.

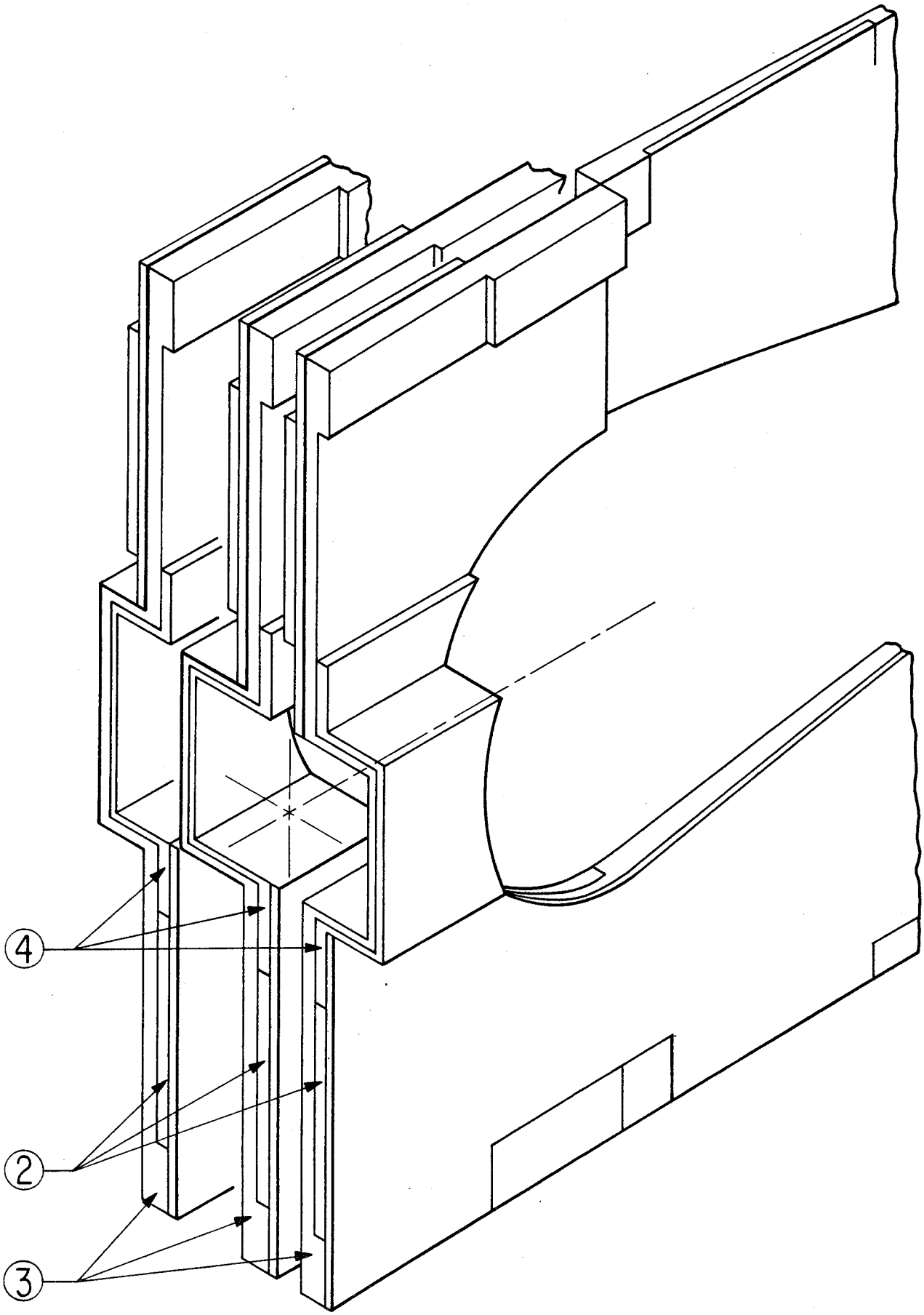

Figure 5.2.2 Port design. Elevation view.

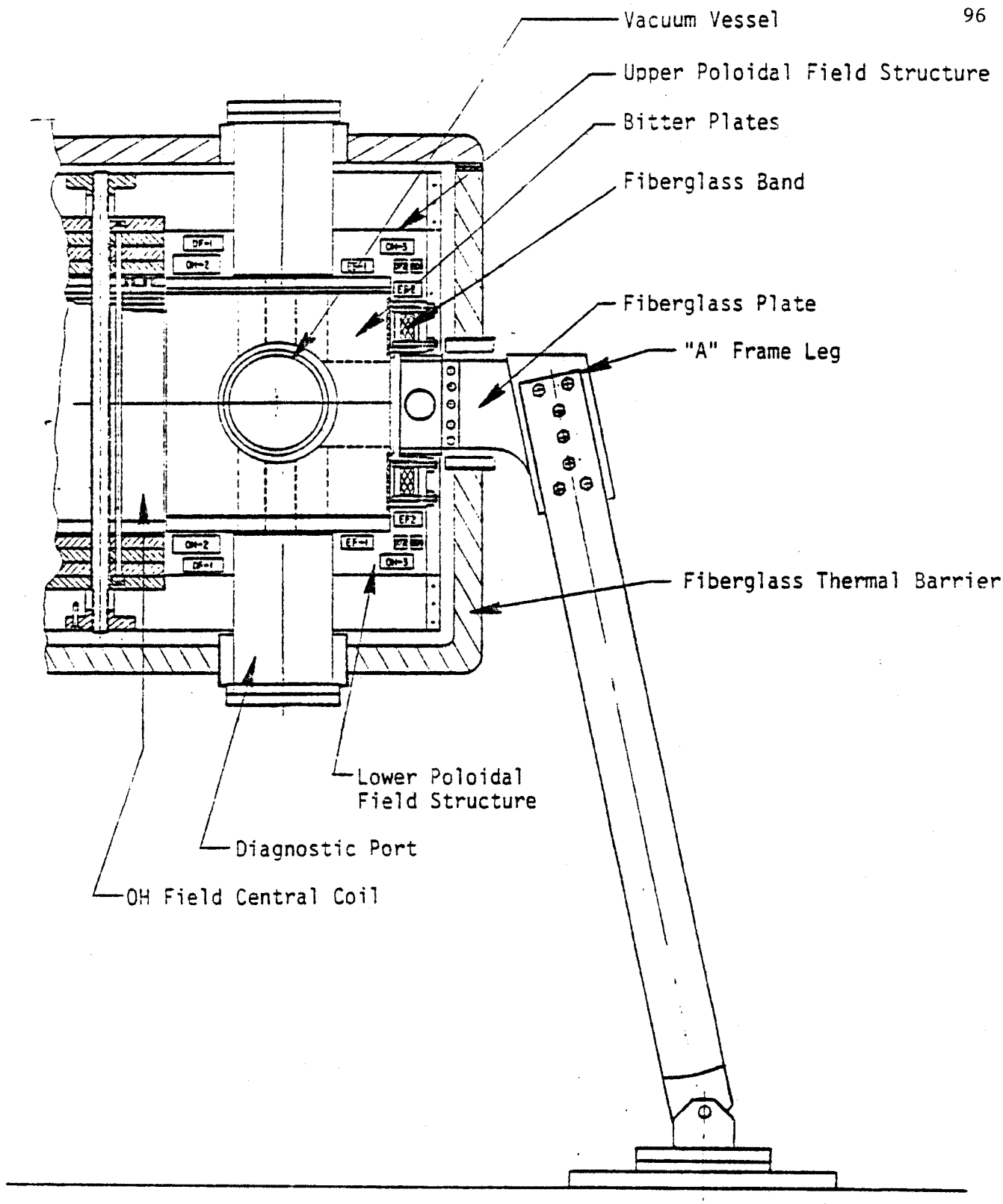

Figure 5.3.1 Elevation — Alcator C

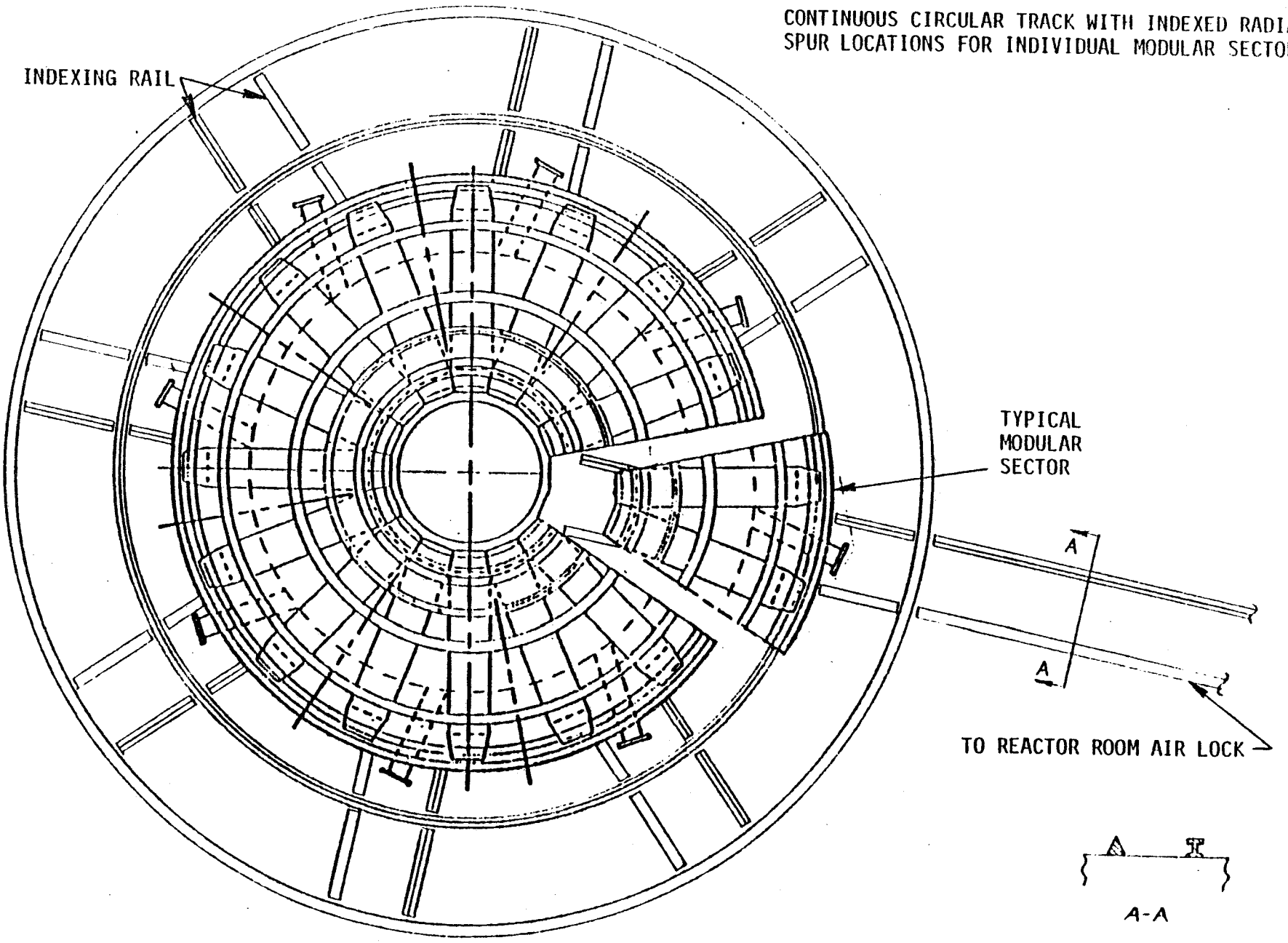

Figure 5.3.2 Plan View Showing Rail System for Mobile Floor Units

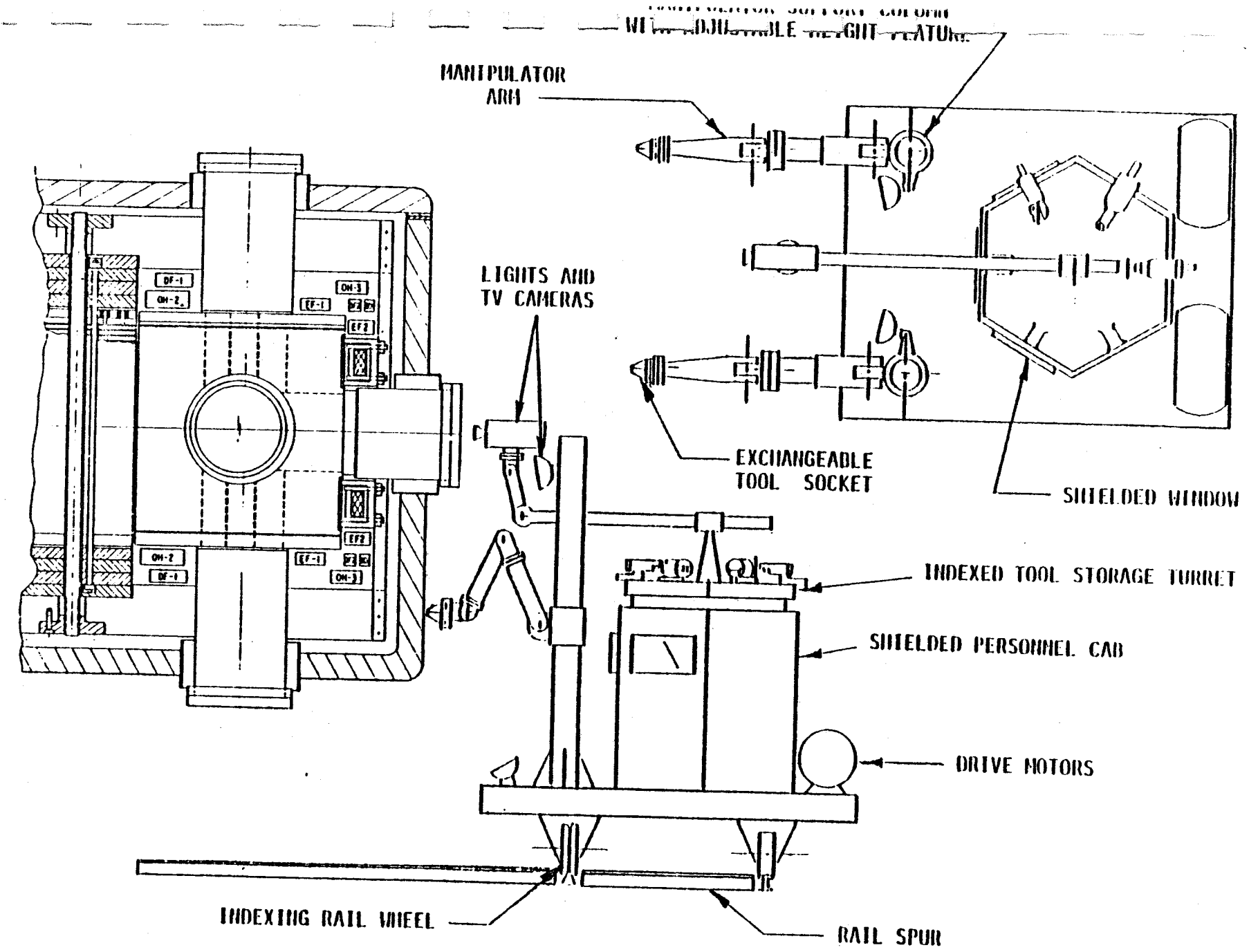

Figure 5.3.3 Shielded Mobile Floor Unit

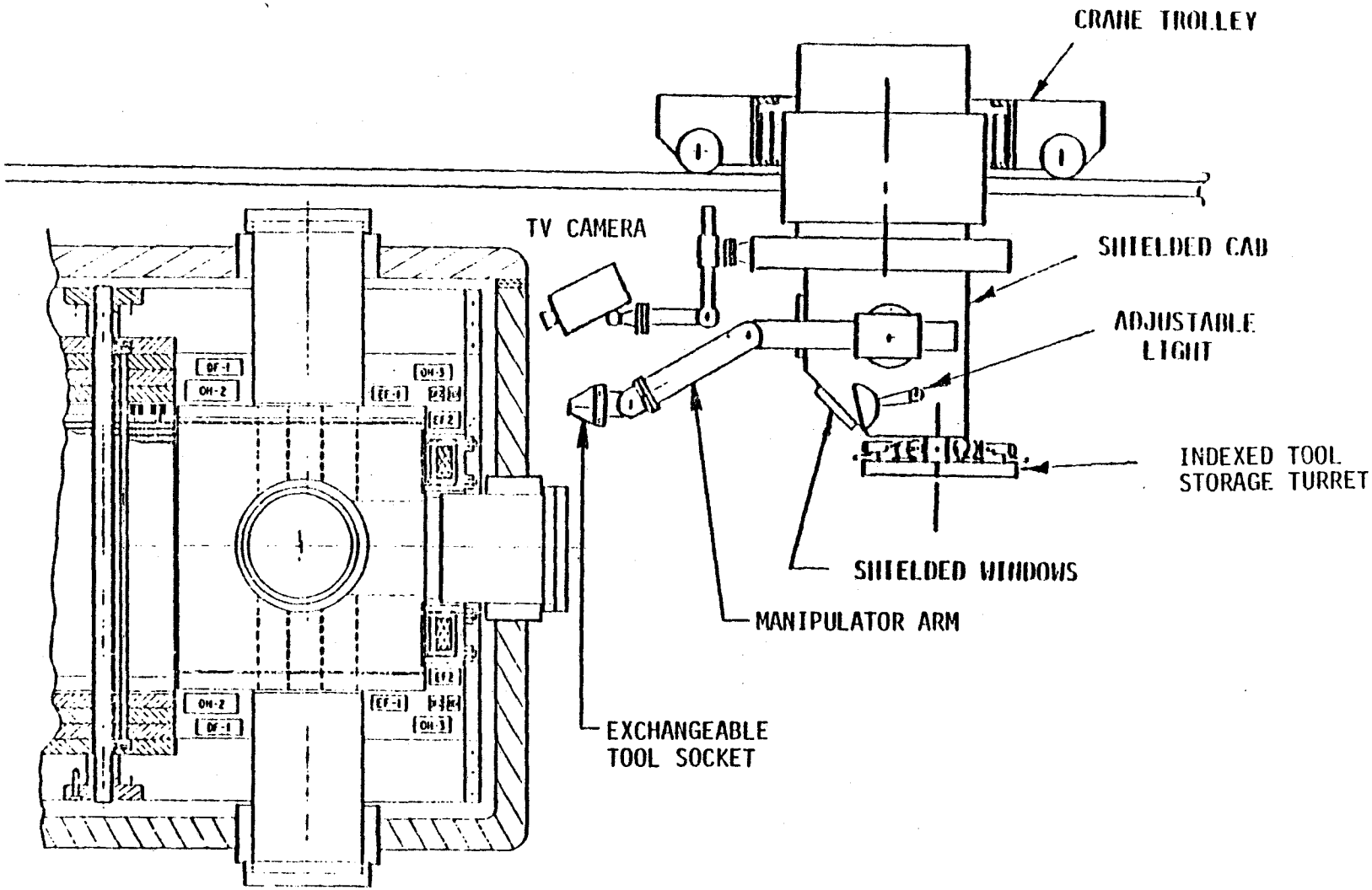

Figure 5.3.4 Shielded Crane Cab

6.0 Vacuum Chamber

The vacuum chamber of an ignited Tokamak must satisfy a number of operational requirements, some of which impose widely disparate demands on design.

The vacuum chamber must combine the following characteristics:

1. It must allow a base vacuum of 10^{-9} torr to be achieved.
2. It must support atmospheric loads and loads due to the interaction of induced currents with the magnetic fields.
3. It must present the highest possible resistance to toroidal currents shunting the plasma current.
4. It must withstand heating from the plasma with the lowest possible temperature rise.
5. It must allow penetration of equilibrium fields in characteristic times short compared with compression times (50 ms).

Additionally, the vacuum chamber of a compressionally heated Tokamak must satisfy these requirements in a shape considerably more difficult to fabricate than the simple circular cross secton needed for an uncompressed plasma.

Basically, three forms of vacuum chamber are open to consideration -- all of them having the pear-shaped cross section shown in Figure 6.0.1 .

1. Thick walled A stainless steel vessel with a 1 cm thick wall would easily satisfy all requirements except 3 and 5. Plasma heating would be tolerated by the thermal inertia of the material and stress problems would be slight. Bake out for high base vacuum would not be particularly difficult. However, the requirement of low current induced by *OH* fields could not be met without an insulating section, presumably ceramic. This would add difficulty to manufacture and unreliability in operation. Furthermore, the *EF* field which rises rapidly during the compression

stage would be significantly distorted even with an insulator to break the toroidal current path.

2. Thin walled, cooled. In this configuration the vacuum vessel is basically a bellows whose convolutions are deep enough to support the load due to external atmospheric pressure. The bellows is cooled on its outer surface by free convection to a liquid coolant (probably water). The plasma heating load is distributed over a large surface area and can be absorbed by free convection boiling in the coolant. The toroidal resistance is sufficiently high so that no insulating spacers need be inserted.
3. Thin walled, shielded. In this arrangement the same bellows as in 2 is used but the external coolant is eliminated. It is replaced by shielding rings located in the vacuum space between the vacuum chamber and the plasma. These rings are 1 cm thick and each is a few centimeters long in the toroidal direction. The periodic discontinuity in the toroidal direction allows the vertical field to penetrate. Direct line of sight heating of the bellows is eliminated by overlapping the rings. This arrangement has the additional advantage of protecting the bellows from plasma disruptions or runaway electrons. It has the disadvantage of more complex construction and possible contamination of the plasma as the shielding rings heat up.

Of these three types of chamber only 2 and 3 above have been considered. Both employ a bellows vacuum chamber and the stresses in this have been particularly examined.

6.1 Thin Walled Chamber with Cooling

A possible form of a thin walled vacuum chamber is shown in Figure 6.0.1. The dimensions allow 2 cm between the inner wall and the plasma. The wall is cooled on its outer surface: water cooling has been examined to determine the feasibility of cooling in general. Compatibility between the cooling method and the liquid nitrogen cooling of the *TF* coil has not been examined.

The wall consists of a convoluted stainless steel bellows. As shown in Figure 6.0.1 the

bellows is made by edge welding pear-shaped hoops which have themselves been formed by welding flat strips at points W. This may not be the best or only method of fabrication, but it is feasible and is indeed used in the manufacture of high extension bellows. The quality control of the welding operation must be particularly high as the total length of weld in the whole chamber is 2.5 km. However, the welding is basically simple and largely automatic. This type of bellows was used in the *ATC* tokamak at PPPL.

The convolutions must be sized so that stresses (bending at P,R and S of Fig. 6.0.1) are limited to values appropriate to welded stainless steel. At present it is considered that 340 MP is a suitable design stress.

The characteristic dimensions of the bellows are material thickness t, convolution height h and pitch a and all three can be sized to control stresses. In practice, however, t must be constant everywhere and a small fraction of the pitch a. The latter varies as the major radius and in practice only h is free to be adjusted independently. However, the ability to adjust h is an important advantage of the edge welded form of constructon for the following reason. In order to minimize size, costs and power of the *ITR*, the *TF* coil must fit as closely as possible to the plasma surface: this is critically important at the compressed plasma position. Thus at the point S, the height h of the convolutions should be as small as possible. However, because of the toroidal geometry, the atmospheric load on one convolution increases with the major radius. Therefore in order to keep the stresses everywhere no greater than at S, the height of the convolutions is increased with major radius.

The number of convolutions per unit length in the toroidal direction affects not only the strength but also the electrical resistance and the allowable thermal load. As a decreases, both the cooling surface area and resistance shunting the plasma increase.

6.1.1. Stresses

The greatest stress (compressive) is at the point S. This stress is generated mainly by atmospheric load although small pulsed electro-magnetic loads are also superimposed. The peak

compressive stress at S is given by

$$\sigma_T = \left(\frac{1.50}{h} + \frac{1.93}{h^2} \right) \frac{a}{t} p \qquad (6.1.1)$$

where p is in Pascals, h is in meters, and a is the pitch of the bellows at S. Suitable values for these main dimensions as follows:

t = 2mm,

a = 10 mm (at S)

a = 23.2 mm (at P)

h = 55. mm (at S)

h = 70. mm (at R)

h = 85. mm (at P)

These parameters lead to a peak compressive stress of 332 MP (48800 psi). The peak tensile stress is 304 MP (44200 psi). The stresses at P are almost the same. This is considered to be sufficiently conservative for type 304 SS edge welded with chills.

6.1.2. Surface Temperature

The inner wall of the bellows is subjected to 17 MW of heating during the plasma ignited phase. It is assumed that half of this flux will be distributed over the bellows segment between T and U (see Figure 6.1.1). Then the heat flux normal to the surface of the convolutions will be 20 w/cm^2. This appears to be sufficiently low that simple forms of liquid contact cooling could be used. The rise of surface temperature would be insignificant.

If, however, confined coolants must be used in tubes attached to the convolutions, hot spots will develop at points remote from the cooling tubes. In order to limit the temperature rise to about 800^0 C, tubes would have to be attached to the middle and edges of each convolution, a form of construction that appears to be very difficult. Although the surface area of the convolutions is large the heat flux may not be incident uniformly. In particular the edges of the 2 mm thick stainless convolutions may intercept 20% of the heat flux. This would then be conducted along the adjacent

convolution to be transferred to the coolant in the region G. The hot spot temperature is given roughly by

$$T_{max} = q\,(k\,t\,\gamma)^{-1/2} \qquad (6.1.2)$$

where k is the thermal conductivity, γ is the heat transfer coefficient and q is the heating flux per unit length of the edge of the convolution. This gives a value for T_{max} of about 200° C.

6.1.3. Temperature Rise.

The volume of a water jacket giving 1 cm clearance over the outer edge of the convolutions is 2.3 m^3. During a 10 second burn the temperature rise will be 17° C.

6.1.4. Electrical Resistance

The shunt resistance of the bellows in parallel with the plasma current is about 2.2 mΩ. This assumes that 10% of the vacuum chamber is occupied by flanges and ports of low resistance. This resistance can be increased by decreasing a or increasing the radial width of the convolutions. Both of these also decrease the stresses.

.6.1.5. Ulage Volume

Because the cost and difficulty of the toroidal field coil is strongly dependent on the distance between its inside surface and the plasma boundary, the radial extent of the bellows is a critical dimension in the system design (see section 2.1).

The present design of bellows requires 5.5 cm for the depth of convolution. An additional 2 cm is allowed for the limiter, and 1 cm for cooling jacket surrounding the bellows. This leaves 1.5 cm between the water jacket and TF coil for insulation.

6.2 Thin Walled Chamber, with Shielding

An alternate first wall concept which has only briefly been considered so far might involve placing heavy overlapping shield rings inside the thin wall bellows chamber. These rings would act like a distributed limiter receiving the plasma power lost by convection and radiation. It is

necessary that these rings overlap to prevent line of sight exposure of vacuum wall, but they must not overlap electrically. If the rings have a 1 centimeter depth, their temperature would rise 27° C/second during the burn. They would cool by radiation and by conduction through their supports following the pulse.

The rings have the advantage of distributing the limiter material, thus preventing local melting due to poor plasma positioning. The uncooled internal rings, however, will experience a significant temperature excursion during the pulse which may have an adverse effect on light element impurity generation. At present it is not considered feasible to directly cool the internal rings.

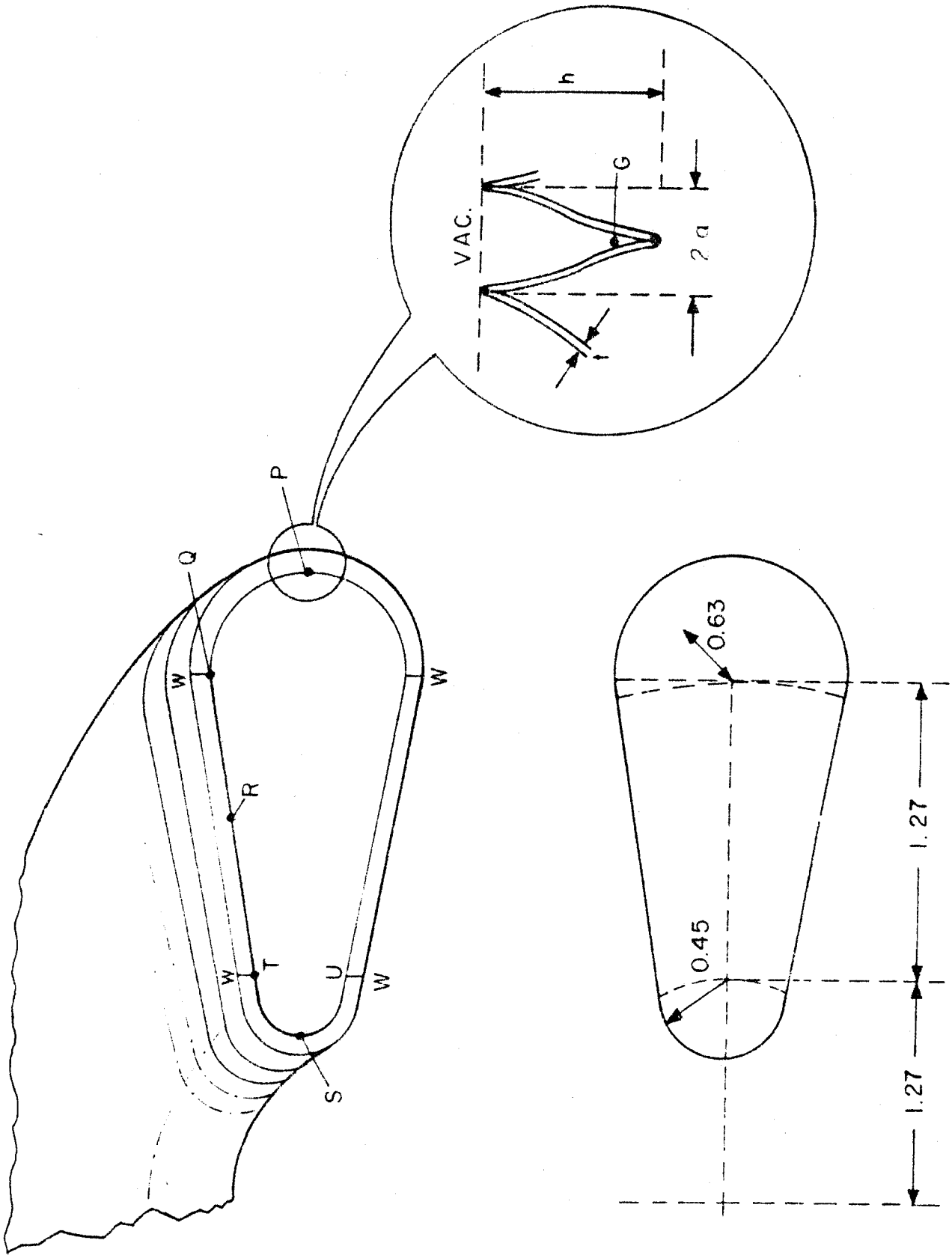

Figure 6.0.1 Conceptual design of vacuum wall.